Arctic ice-ocean simulation with optimized model parameters: Approach and assessment

An T. Nguyen,[1,2] Dimitris Menemenlis,[2] and Ronald Kwok[2]

Received 3 August 2010; revised 3 December 2010; accepted 25 January 2011; published 27 April 2011.

[1] We present an optimized 1992–2008 coupled ice-ocean simulation of the Arctic Ocean. A Green's function approach adjusts a set of parameters for best model-data agreement. Overall, model-data differences are reduced by 45%. The optimized simulation reproduces the negative trends in ice extent in the satellite records. Volume and thickness distributions are comparable to those from the Ice, Cloud, and land Elevation Satellite (2003–2008). The upper cold halocline is consistent with observations in the western Arctic. The freshwater budget of the Arctic Ocean and volume/heat transports of Pacific and Atlantic waters across major passages are comparable with observation-based estimates. We note that the optimized parameters depend on the selected atmospheric forcing. The use of the 25 year Japanese reanalysis results in sea ice albedos that are consistent with field observations. Simulated Pacific Water enters the Bering Strait and flows off the Chukchi Shelf along four distinct channels. This water takes ~5–10 years to exit the Arctic Ocean at the Canadian Arctic Archipelago, Nares, or Fram straits. Atlantic Water entering the Fram Strait flows eastward, merges with the St Ana Trough inflow, and splits into two branches at the southwest corner of the Makarov Basin. One branch flows along Lomonosov Ridge back to Fram Strait. The other enters the western Arctic, circulates cyclonically below the halocline, and exits mainly through the Nares and Fram straits. This work utilizes the record of available observations to obtain an Arctic Ocean simulation that is in agreement with observations both within and beyond the optimization period and that can be used for tracer and process studies.

Citation: Nguyen, A. T., D. Menemenlis, and R. Kwok (2011), Arctic ice-ocean simulation with optimized model parameters: Approach and assessment, *J. Geophys. Res.*, *116*, C04025, doi:10.1029/2010JC006573.

1. Introduction

[2] Global coupled ocean and sea ice models are widely used to study the responses of the ocean and sea ice to climate change. Existing model-data comparisons show large systematic differences in the character of the principal water masses in the Arctic Ocean. Some of the most common model shortcomings include the lack of a cold halocline in the Amerasian Basin, misrepresentations and systematic drifts in the core temperature of the Atlantic Water, and discrepancies in hydrographic and sea ice transports by factors of two or higher across Fram Strait [*Holloway et al.*, 2007; *Martin and Gerdes*, 2007; *Holland et al.*, 2006; W. Maslowski, personal communication, 2009]. These shortcomings are in part the result of the models' inability to resolve eddies and eddy-driven dynamics due to their limited horizontal resolution (50 to 100 km) and in part the result of unmodeled physics such as shelf water formation and tides [*Holloway et al.*, 2007]. The prevalent model-data discrepancies can be identified using assessment metrics and sensitivity studies to models parameters.

[3] Previous attempts to incorporate data into model simulations in the polar region have focused primarily on adjusting either the sea ice or ocean system without considering their coupled behavior, [e.g., *Zhang et al.*, 2003; *Lindsay and Zhang*, 2006; *Harder and Fischer*, 1999; *Miller et al.*, 2006]. For sea ice, Kalman filters and optimal interpolation techniques are typically used to minimize differences between model and buoy/satellite ice drifts and concentration [e.g., *Zhang et al.*, 2003; *Lindsay and Zhang*, 2006; *Stark et al.*, 2008; *Rollenhagen et al.*, 2009]. There are also studies that aimed to adjust model parameters such as ice albedos, drag coefficients, and strengths in stand-alone ice models using Monte Carlo approaches [e.g., *Harder and Fischer*, 1999; *Miller et al.*, 2006]. These studies utilized hundreds of sensitivity experiments to narrow down the optimal sets of parameters. Often, non-uniqueness can result in multiple sets of parameters depending on initial and boundary conditions. In the ocean, 3D-Var and 4D-Var methods have been used to assimilate observed oceanic temperature and salinity to reconstruct

[1]Joint Institute for Regional Earth System Science and Engineering, University of California, Los Angeles, California, USA.
[2]Jet Propulsion Laboratory, California Institute of Technology, Pasadena, California, USA.

0148-0227/11/2010JC006573

Table 1. Data Used in the Optimization Procedure

Data Type	Spatial Coverage	Temporal Coverage	Accuracy	Description	Source
Sea ice					
Velocity	Arctic	1992–2002	±0.03 m/s	passive microwave	http://www-radar.jpl.nasa.gov/rgps/
Fluxes	FS	1992–2002	±17,000–25,000 km^{2a}	passive microwave	*Kwok and Rothrock* [1999] and *Kwok et al.* [2004]
	CAA	1997–2002	±110 km^{2a}		*Kwok* [2006]
Thickness	Arctic	1992–2002	0.29 ± 0.25 m, 0.75 m^{b}	Submarine ULS	http://www.nsidc.org
	Gr/No seas	1991–2002	±0.20 m	AWI ULS mooring	*Witte and Fahrbach* [2005]
Concentration	Arctic	1992–2007	±10%	SSMI	*Comiso et al.* [1997]
Extent	Arctic	1992–2007	±10%	SSMI	*Comiso et al.* [1997]
Ocean					
CTD	Arctic	1993–2000	0.001–0.005°C	SCICEX	http://www.ldeo.columbia.edu/res/pi/SCICEX
	Gr/No seas and FS	1996–2006	salinity ±0.005	ASOF	http://www.pangaea.de/
	Beaufort Sea	2002–2003	salinity ±0.005	BGEP	http://www.whoi.edu/beaufortgyre/
Currents	FS	1996–2006	±0.01 m/s	ASOF	*Fahrbach et al.* [2001]
Fluxes					
Heat	FS	1996–2006	±5–6 TW	ASOF	*Schauer and Fahrbach* [2004]
Freshwater	FS	1996–2006	±1–2 Sv	ASOF	*Schauer and Fahrbach* [2004]
Heat	BS	1990–2004	±30%	mooring	*Woodgate et al.* [2006] and *Woodgate and Aagaard* [2005]
Volume	BS	1990–2004	±10–15%	mooring	*Woodgate et al.* [2006] and *Woodgate and Aagaard* [2005]
Freshwater	BS	1990–2004	±10–15%	mooring	*Woodgate et al.* [2006] and *Woodgate and Aagaard* [2005]

[a]Uncertainties are reported per winter (October–May).
[b]Here 0.75 m for U.S. former classified data and 0.25 m for the rest of the ULS data.

regional or basin-wide circulation patterns [e.g., *Nechaev et al.*, 2004; *Panteleev et al.*, 2010]. In all the above efforts, the ocean and sea ice data assimilations are not coupled.

[4] In contrast to above studies, we use a Green's function approach to obtain an optimal set of ocean and sea ice model parameters for a coupled ocean and sea ice Arctic Ocean. In this paper, we provide an assessment of the "baseline" and of the "optimized" Arctic Ocean simulations. The baseline simulation exhibits many common issues identified by *Holloway et al.* [2007] and *Holland et al.* [2006]. The optimized simulation reduces model-data difference by 45%. Additionally, this simulation does not contain discontinuities when and where data are ingested, as would be the case, for example, if a Kalman filter or an optimal interpolation approach had been used. Therefore the optimized simulation is suitable for budget analyses and for tracer studies [e.g., *Manizza et al.*, 2009].

[5] The paper is organized as follows. Section 2 describes the data sets used in the optimization and in the assessment of the simulations. Section 3 discusses the Green's function approach, the MITgcm model configuration, and the optimized parameters. In section 4, we present the assessment of the models' sea ice and ocean water properties and, when available, compare our solution with those from the Arctic Ocean Models Intercomparison Project (AOMIP). Our model's strengths and weaknesses are assessed and future directions are discussed in section 5.

2. Data

[6] Data used in this assessment are sea ice velocity, fluxes, area, thickness, oceanic vertical conductivity-temperature-depth (CTD) profiles, and oceanic heat and volume transports. Table 1 lists the data types, their spatial and temporal coverage, and expected quality. Data uncertainties are briefly discussed here and are used when considering the least squares weights in section 3.2.

2.1. Sea Ice Drafts

[7] The U.S. Navy and Royal submarine upward looking sonar (ULS) ice draft from 1975 to 2000 is the only data set with long temporal coverage and it covers over half of the central Arctic [*Rothrock and Wensnahan*, 2007]. Individual 10–50 km section of the averaged ice draft has an expected bias of 0.29 m with an expected uncertainty of 0.25 m [*Rothrock and Wensnahan*, 2007]. In addition to the submarine data, In addition to the submarine data, the Alfred Wegener Institute (AWI) Moored ULS data set, which covers the Fram Strait and Greenland/Norwegian seas (Gr/No), for the 1992–2002 period is used [*Witte and Fahrbach*, 2005]. Individual AWI ice draft measurement has an accuracy of ±0.20 m [*Witte and Fahrbach*, 2005]. We average the data into ~20 km sections using a typical sea ice speed of 0.1 m/s prior to comparing with model output. Drafts are converted to thickness by multiplying with a factor of 1.1, which is approximately the ratio of mean seawater density of 1024 kg/m^3 and sea ice density of 910 kg/m^3. The mean and standard deviation of ice drafts within each 20 km section are shown in Figures 4a and 4b. The ice draft standard deviations are ~1 m in the Gr/No seas and 1–2 m in the Arctic Ocean.

2.2. Sea Ice Velocity

[8] Optimally interpolated ice motions at horizontal resolution 12.5 × 12.5 km^2 from 1992–2003 can be downloaded at http://www-radar.jpl.nasa.gov/rgps/ice_motion_3.html [*Kwok et al.*, 1998]. The optimally interpolated data set combines ice motion buoys and passive microwave from both 37 GHz and 85 GHz channels. Overall, the error in sea ice velocity is 4.4–6.7 km/d [*Kwok*, 2009]. Additionally, we use monthly averaged velocity fields to assess the model

large-scale velocity patterns. In this case, we expect the standard errors to be $\sigma_t/\sqrt{N} \approx 0.80$ km/d or 0.01 m/s where $N = 30$ is the number of days per month.

2.3. Sea Ice Fluxes

[9] Winter sea ice fluxes across Fram Strait and the Canadian Arctic Archipelago (CAA) provide constraints to the Arctic ice exports and hence influence the sea ice and freshwater mass budgets. Fluxes are derived from passive microwave and RADARSAT Synthetic Aperture Radar images for the 1992–2002 period and are calculated across gates as defined by *Kwok et al.* [2004] and *Kwok* [2006]. Across Fram Strait, uncertainties per winter (October–May) are 17,000–25,000 km^2 for area flux and 100–240 km^3 for volume flux [*Kwok and Rothrock*, 1999]. Across the CAA, uncertainties in area flux are ~110 km^2 per winter [*Kwok*, 2006].

2.4. Sea Ice Concentration

[10] Satellite sea ice concentration from the bootstrap technique [*Comiso et al.*, 1997] is available on a 25 km horizontal grid at http://nsidc.org. Uncertainties in sea ice concentration are between 4 to 7% during the winter and are higher during the summer months [*Kwok*, 2009; *Spreen et al.*, 2008]. We use concentration primarily to evaluate gross model biases in seasonal ice zones.

2.5. Conductivity Temperature Depth Profiles

[11] CTD measurements from the Scientific Ice Expeditions (SCICEX) [*Langseth et al.*, 1993; *Hopkins et al.*, 1998; *Boyd et al.*, 1998; *Edwards et al.*, 1999; *Rothrock et al.*, 1999] and the Beaufort Gyre Exploration Project (BGEP) [*Kemp et al.*, 2005] are downloaded from http://www.ldeo.columbia.edu/, http://nsidc.org, and http://www.whoi.edu/beaufortgyre/. Temporal coverages are from 1993–2000 for SCICEX and 2003–2004 for BGEP data. Measurement accuracies are ±0.005°C for temperature and ±0.005 for derived salinity. Our aim is to capture the large basin-scale water mass properties using this data set. In dealing with differences between data and model temporal (daily versus monthly) and spatial (point measurement versus 18 km × 18 km areal average) coverage, we always interpolate model results to the data locations.

2.6. Mooring Current Meters, Volume, and Heat Fluxes

[12] Current meters and estimated volume/heat fluxes across Fram Strait [*Fahrbach et al.*, 2001; *Schauer and Fahrbach*, 2004] and across Bering Strait [*Woodgate and Aagaard*, 2005; *Woodgate et al.*, 2006] are used to assess heat and volume transports and budgets in the Arctic. Velocity across Fram Strait is sampled hourly from September 1997–2000 in 14 profiles. Temperature and salinity (T/S) vertical profiles are sampled at finer horizontal resolutions and are used to derive heat and volume fluxes. Uncertainties are on the order of 0.5–1.0 cm/s for velocity [*Fahrbach et al.*, 2001], 1–2 Sv for volume transport, and 5–6 TW for heat transport [*Schauer and Fahrbach*, 2004]. Across Bering Strait, uncertainties are 20–30% in net heat and 10–15% in net volume fluxes [*Woodgate et al.*, 2006; *Woodgate and Aagaard*, 2005].

2.7. Atmospheric Boundary Conditions

[13] Atmospheric boundary conditions considered in this study include the European Center for Medium-Range Weather Forecasts (ECMWF) 40 year reanalysis (ERA-40) and the Japanese 25 year Reanalysis Project (JRA25). JRA25 covers 1979–2004 and is described by *Onogi et al.* [2007]. The Japan Meteorological Agency (JMA) Climate Data Assimilation System (JCDAS) provides a near real-time analysis that is consistent with the JRA25 reanalysis starting in January 2005. Therefore using the JRA25/JCDAS atmospheric fields allows near real-time ocean-ice simulations. Section 3.5 discusses in more detail the effect of atmospheric boundary conditions on the simulation results.

3. Optimization

3.1. Green's Function Approach

[14] Green's functions provide a simple yet effective method to adjust general circulation model (GCM) parameters [*Menemenlis et al.*, 2005a]. The Green's function approach involves the computation of GCM forward sensitivity experiments for each parameter that is to be adjusted followed by a recipe for constructing a solution that is the best linear combination of these sensitivity experiments. Technically, Green's functions are used to linearize the GCM and discrete inverse theory [*Menke*, 1989] is used to estimate the GCM parameters. A short description of the Green's function approach follows using the notation of *Wunsch* [2006].

[15] An ocean general circulation model can be thought of as a set of rules for time stepping an ocean state vector $\mathbf{x}(t)$ one time step Δt into the future

$$\mathbf{x}(t + \Delta t) = M(\mathbf{x}(t), \boldsymbol{\eta}). \tag{1}$$

State vector $\mathbf{x}(t)$ includes ocean temperature, salinity, and velocity and sea ice thickness, concentration, and velocity on the model grid at time step t. Function M represents the numerical model and vector $\boldsymbol{\eta}$ contains model parameters, for example, initial and surface boundary conditions, subgrid-scale mixing, albedos, and drag coefficients. Parameters in $\boldsymbol{\eta}$ are not known exactly. We assume that they can be represented by a white noise process with mean $\boldsymbol{\eta_o}$ and covariance matrix $\mathbf{Q}$.

[16] The observation equation relates state vector $\mathbf{x}$ to observations $\mathbf{y}$ through operator H

$$\mathbf{y} = H(\mathbf{x}) + \boldsymbol{\epsilon}, \tag{2}$$

where vector $\mathbf{x}$ now represents the complete time history of the state vector, i.e.,

$$\mathbf{x}^T = \left[\mathbf{x}(t)^T \;\; \mathbf{x}(t + \Delta t)^T \;\; \mathbf{x}(t + 2\Delta t)^T \;\; \ldots\right]. \tag{3}$$

Vector ϵ is the observation noise process, which is assumed Gaussian with zero mean and covariance $\mathbf{R}$. Equation (2) can also be written in terms of parameter vector $\boldsymbol{\eta}$

$$\mathbf{y} = G(\boldsymbol{\eta}) + \boldsymbol{\epsilon}, \tag{4}$$

where G represents the convolution of ocean model M and measurement model H. To solve the highly nonlinear

Table 2. Model Parameters Used in Baseline **A0**, Optimized **A1**, and AOMIP Experiments

Parameter	A0	A1	AOMIP[a]	Comment
Initial conditions	ECCO2	WOA05		Fields considered include PHC, WOA05, WOA01, WGHC
Atmospheric forcing	ECCO2	JRA25		ECCO2 was based on ERA40/ECMWF
Ocean albedo	0.15	0.16 ± 0.04	0.10	
Sea ice dry albedo	0.88	0.7	0.6–0.75	0.73–0.83 from the Community Climate System Model (CCSM)[b]
Sea ice wet albedo	0.79	0.71 ± 0.08	0.5–0.68	≥0.655 from CCSM 0.4–0.6 from *Curry et al.* [2001]
Snow dry albedo	0.97	0.87 ± 0.10	0.80–0.84	0.96 from CCSM 0.84 from *Curry et al.* [2001]
Snow wet albedo	0.83	0.81 ± 0.10	0.60–0.77	≥0.86 from CCSM 0.77 from *Curry et al.* [2001]
Ocean/air drag	1.02	1.00 ± 0.05		
Air/sea ice drag	0.0020	0.0011 ± 0.0003	0.0011–0.0013	
Ocean/sea ice drag	0.0052	0.0054 ± 0.0001	0.0055	
Ice strength P^*	2.7	2.3 ± 1.2	1.0–2.75	10^4 Nm^{-2}
Lead closing H_o	0.5	0.6 ± 0.7	0.25–0.5	
Vertical diffusivity	10^{-5}	5.44×10^{-7}		m^2/s
Salt plume	off	on		*Nguyen et al.* [2009]
River runoff factor	1	1.2 ± 1.2		factor × ARDB[c]

[a] *Martin and Gerdes* [2007] and *Johnson et al.* [2007].
[b] Arctic Runoff Database and P. Winsor (personal communication, 2007).
[c] Community Climate System Model, version 3 [*Briegleb et al.*, 2004]. Values listed for spectrum with wavelengths <0.7 μm and are typically ~0.3 higher than those in with wavelengths >0.7 μm.

equation (4) for $\boldsymbol{\eta}$, we linearize it around a baseline ocean model integration, i.e., we integrate equation (1) with our best prior estimate $\boldsymbol{\eta_o}$ of the model parameters, and we rewrite the observation equation as

$$\boldsymbol{\Delta y} = \mathbf{G}\,\boldsymbol{\Delta\eta} + \boldsymbol{\epsilon}, \tag{5}$$

where $\boldsymbol{\Delta\eta} = \boldsymbol{\eta} - \boldsymbol{\eta_o}$ and $\boldsymbol{\Delta y} = \mathbf{y} - G(\boldsymbol{\eta_o})$. Matrix $\mathbf{G}$ is the Jacobian matrix $\partial \boldsymbol{y}/\partial \boldsymbol{\eta}$. Each column of matrix $\mathbf{G}$ can be computed using a model perturbation experiment, i.e., a model Green's function for the corresponding parameter in vector $\boldsymbol{\eta}$.

[17] A cost function J that measures the length of the control parameter perturbation and of the model-data misfit is defined

$$J = \boldsymbol{\Delta\eta}^T \mathbf{W}_\eta\, \boldsymbol{\Delta\eta} + (\boldsymbol{\Delta y} - \mathbf{G}\boldsymbol{\Delta\eta})^T \mathbf{W}_y\, (\boldsymbol{\Delta y} - \mathbf{G}\boldsymbol{\Delta\eta}), \tag{6}$$

where $\mathbf{W}_\eta$ and $\mathbf{W}_\mathbf{y}$ are weight matrices for the control parameter perturbation $\boldsymbol{\Delta\eta}$ and the model-data misfit $\boldsymbol{\Delta y} - \mathbf{G}\boldsymbol{\Delta\eta}$, respectively. If the model and observation error covariance matrices are known, minimizing J with $\mathbf{W}_\eta = \mathbf{Q}^{-1}$ and $\mathbf{W}_\mathbf{y} = \mathbf{R}^{-1}$ provides the maximum likelihood estimate [*Menke*, 1989; *Wunsch*, 2006]. The minimization of cost function J with respect to $\boldsymbol{\Delta\eta}$ yields the solution

$$\widetilde{\boldsymbol{\Delta\eta}} = \left(\mathbf{G}^T \mathbf{W}_\mathbf{y}\, \mathbf{G} + \mathbf{W}_\eta\right)^{-1} \mathbf{G}^T \mathbf{W}_\mathbf{y}\, \boldsymbol{\Delta y}. \tag{7}$$

[18] An estimate of ocean circulation is then obtained by integrating the model equation (1) using parameters $\tilde{\boldsymbol{\eta}} = \boldsymbol{\eta_o} + \widetilde{\boldsymbol{\Delta\eta}}$. For global ocean models, the length of the parameter vector $\boldsymbol{\eta}$ can exceeds 10^9. Therefore the computation of the full Jacobian matrix $\mathbf{G}$ using a Green's function approach and the inversion of $\mathbf{G}$, as required in equation (7), would be prohibitive. Nevertheless, as demonstrated herein and by *Menemenlis et al.* [2005a], the optimization of a small number of carefully chosen parameters $\boldsymbol{\eta}$ can lead to a substantial reduction of cost function J.

3.2. Error Covariances and Weights

[19] We consider three different alternatives for weight matrix $\mathbf{W}_\mathbf{y}$ in the cost function, equation (6), because a prior data error covariances are not known and are difficult to estimate. In the first option each data set is assigned weights that are inversely proportional to the number of data points within that set, i.e., we divide each data set by the number of data points in that particular set. In the second option, weights are assigned such that each data set has approximately equal contribution to the overall cost function. In the third option, we scale each term of the cost function by the variance of the model-data difference. Admittedly, all three weight matrices are arbitrary and all three ignore the spatial and temporal covariances in the errors, i.e., the off-diagonal elements in $\mathbf{W}_\mathbf{y}$ are set to zero. Of interest to the present discussion is that the three cases are different and that they allow us to explore a wide range of plausible solutions. The results presented in Table 2 are based on the second option, that is, $\mathbf{W}_\mathbf{y}$ is a diagonal matrix with scaling factors chosen so that the respective contributions of each data set to the cost function are approximately equal. Given that the number of observations is much larger than the number of model parameters being estimated, we set $\mathbf{W}_\eta$ to zero. That is, we assume that there is no a priori knowledge about the control parameters.

3.3. Baseline simulation A0

[20] The Green's function optimization approach is applied to a regional Arctic Ocean configuration of the Massachusetts Institute of Technology general circulation model (MITgcm) [*Marshall et al.*, 1997]. This configuration is described in detail by *Losch et al.* [2010] and was previously used in the studies of *Condron et al.* [2009],

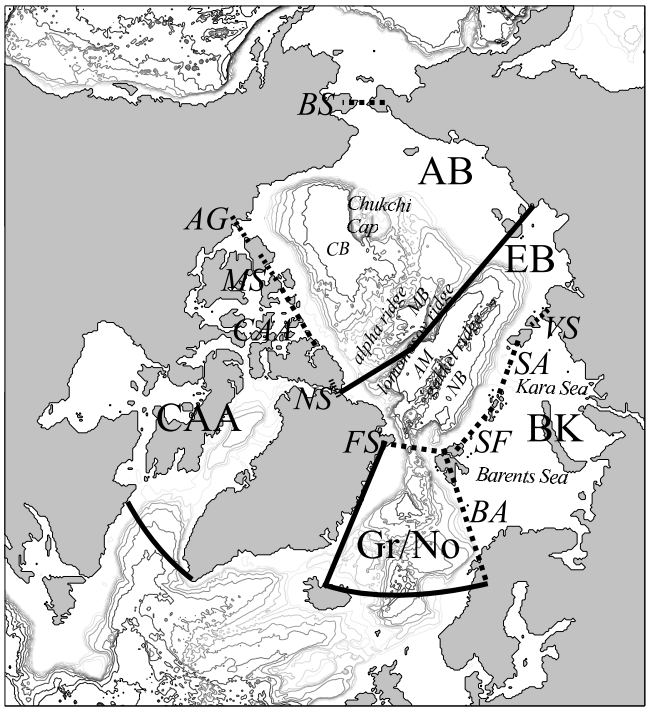

Figure 1. The model Arctic domain showing five regions Amerasian Basin (AM), Eurasian Basin (EB), Barents and Kara seas (BK), Greenland and Norwegian seas (Gr/No), and Canadian Arctic Archipelago (bold CAA). Regions AB and EB are defined by *Holloway et al.* [2007]. Also shown are locations of the individual Nansen Basin (NB), Amundsen Basin (AB), Makarov Basin (MB), and Canada Basin (CB). Gates used in transport calculations are Fram Strait (FS), Barents Sea opening (BA), Svalbard to Franz Josef Land (SF), St Ana Trough (SA), Vilkitshogo Strait (VS), Bering Strait (BS), Amundsen Gulf (AG), McClure Strait (MS), Canadian Arctic Archipelago (italic CAA), and Nares Strait (NS).

Manizza et al. [2009], and *Nguyen et al.* [2009]. The domain of integration is shown in Figure 1; boundaries are at ~55°N in both the Atlantic and Pacific sectors. These boundaries coincide with grid cells in a global, cubed sphere configuration of the MITgcm [*Menemenlis et al.*, 2005b, Figure 1].

[21] The grid covering the Arctic domain is locally orthogonal with horizontal grid spacing of ~18 km. There are 50 vertical levels ranging in thickness from 10 m near the surface to ~450 m at a maximum model depth of 6150 m. The model employs the rescaled vertical coordinate "z*" of *Adcroft and Campin* [2004] and the partial cell formulation of *Adcroft et al.* [1997], which permits accurate representation of the bathymetry. Bathymetry is from the S2004 (W. Smith, unpublished data, 2004) blend of the *Smith and Sandwell* [1997] and the General Bathymetric Charts of the Oceans (GEBCO) one arc minute bathymetric grid. The nonlinear equation of state of *Jackett and McDougall* [1995] is used. Vertical mixing follows the K profile parameterization (KPP) of *Large et al.* [1994]. A seventh-order monotonicity-preserving advection scheme [*Daru and Tenaud*, 2004] is employed and there is no explicit horizontal diffusivity. Horizontal viscosity follows *Leith* [1996] but is modified to sense the divergent flow [*Fox-Kemper and Menemenlis*, 2008].

[22] The ocean model is coupled to the MITgcm sea ice model described by *Losch et al.* [2010]. Ice mechanics follow a viscous plastic rheology and the ice momentum equations are solved numerically using the line successive over relaxation (LSOR) solver of *Zhang and Hibler* [1997]. Ice thermodynamics use a zero heat capacity formulation and seven thickness categories, equally distributed between zeros to twice the mean ice thickness in each grid cell. Ice dynamics use only two thickness categories: open water and sea ice. The model includes prognostic variables for snow thickness and for sea ice salinity.

[23] The baseline (or **A0**) Arctic Ocean integration is derived from a globally optimized simulation, which was generated by the Estimating the Circulation and Climate of the Ocean, Phase II project (ECCO2) [*Menemenlis et al.*, 2008]. This ECCO2 simulation provides initial and lateral boundary conditions, surface atmospheric forcing fields, and various model parameter values for the **A0** integration. In particular, surface boundary conditions are derived from the ERA-40 [*Uppala et al.*, 2005] but have been adjusted during the 1992–2002 period using a global Green's function optimization. Because the ERA-40 reanalysis ends in August 2002, the ECMWF atmospheric analysis is used after August 2002. Six hourly surface winds, temperature, humidity, downward short- and long-wave radiation, and precipitation are converted to heat, freshwater, and wind stress fluxes using the *Large and Yeager* [2004] bulk formulae. Short-wave radiation decays exponentially with depth as per *Paulson and Simpson* [1977]. Low-frequency precipitation has been adjusted using the pentad (5 day) data from the Global Precipitation Climatology Project (GPCP) [*Huffman et al.*, 2001]. Monthly mean river runoff is based on the Arctic Runoff Database (ARDB) as prepared by P. Winsor (personal communication, 2007). Other baseline model parameters, which were used for the **A0** integration, are listed in Table 2.

[24] Despite the global ECCO2 optimization on which it is based, **A0** exhibits many common issues identified by *Holloway et al.* [2007] and *Holland et al.* [2006]. A second Arctic Ocean simulation (called **A1**) based on a regional Green's function optimization is discussed next.

3.4. Optimized Simulation A1

[25] The Green's function approach requires one complete 1992–2004 model integration for each control parameter that is to be adjusted. As a result, only 16 model parameters that are expected to have a large impact on the solution are selected. They include initial conditions, surface boundary conditions, and several ocean and sea ice model parameters. Table 2 provides values for **A0** and **A1**, and for the range of values used in AOMIP. For each parameter we carried out a sensitivity experiment relative to **A0** in order to construct the Jacobian matrix, **G** in equation (5). Data used in the cost function, J in equation (6), include sea ice drift, concentration, thickness, and ocean T/S profiles (see section 2). In addition to adjusted parameters, the **A1** simulation differs from **A0** by the inclusion of the *Nguyen et al.* [2009] salt plume parameterization. This parameterization distributes salt rejected during sea ice formation to the neutral buoyancy

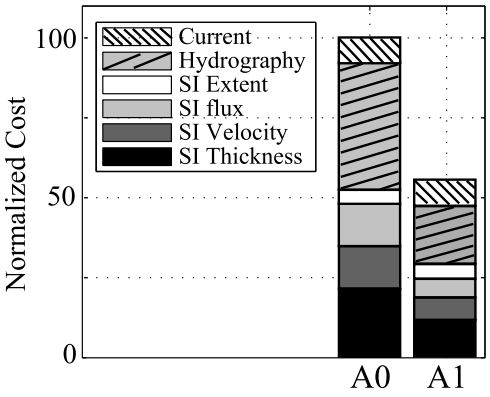

Figure 2. Total cost normalized by the cost of simulation **A0**. Sea ice cost is shown in solid color and oceanic cost in hatched areas. The cost reduction J_2 in simulation **A1** is 44% relative to A0, with ~45% reduction in sea ice cost and 44% reduction in oceanic cost.

depth at the base of the mixed layer and improves the representation of water masses in **A1**.

3.5. Sensitivity Experiments

[26] Initial conditions in Table 2 pertains to initial conditions: a more realistic initial ocean and sea ice state minimizes model drift. The Arctic Ocean model was integrated with initial conditions from the Polar Science Center Hydrographic Climatology (PHC) [*Steele et al.*, 2001], the World Ocean Atlas 2001 (WOA01) [*Conkright et al.*, 1989], the World Ocean Atlas 2005 (WOA05) [*Locarnini et al.*, 2006; *Antonov et al.*, 2006], and the World Ocean Circulation Experiment Global Hydrographic Climatology (WGHC) [*Gouretski and Koltermann*, 2004]. WOA05 yielded the lowest cost and is used for optimized simulation **A1**.

[27] Atmospheric forcing in Table 2 pertains to atmospheric surface boundary conditions. We carried out four sensitivity experiments using atmospheric boundary conditions from the National Centers for Environmental Prediction (NCEP), the Common Ocean Reference Experiments (CORE) [*Large and Yeager*, 2004], the ECCO2/ERA40/ECMWF blend, and the JRA25 [*Onogi et al.*, 2007]. JRA25 yielded the lowest cost and is used for optimized simulation **A1**.

[28] Optimized sea ice and snow albedos are comparable with those used in the AOMIP experiments and with observations (Table 2). The model is insensitive to dry ice albedo as winter ice is mostly snow covered. As a result, we use the AOMIP dry ice albedo of 0.7 in our optimized experiment. The decrease from the high albedos in **A0** to more realistic albedos in **A1** results from using atmospheric boundary conditions from JRA25 instead of the ECCO2/ERA40/ECMWF blend. Specifically, ERA40 overestimates downward short-wave radiation at the surface in high-latitude regions due to inaccuracies in the radiative properties of clouds [*Allan et al.*, 2004]. As a consequence, albedos in experiments with ERA40 atmospheric boundary conditions have to be artificially increased to compensate for the excess downward short-wave radiation.

[29] In addition to albedos, several sea ice parameters including drag coefficients, strength, and lead closing parameters are optimized. Drag coefficients control sea ice drifts and are adjusted to yield reasonable velocity and sea ice/ocean transports [*Harder and Fischer*, 1999; *Miller et al.*, 2006]. The sea ice pressure parameter P* (also known as "strength") affects ice internal strength and dynamics, and is typically adjusted to bring ice motions and thickness to better agreement with observations [*Steele et al.*, 1997]. Lastly, the ice demarcation thickness H_o controls the ice opening/closing rate in leads and polynyas [*Hibler*, 1979] and is adjusted to bring ice thickness and concentration to closer agreement with data. Values of the drag coefficients and of the sea ice strength parameter are consistent with those used in the AOMIP models (Table 2) [*Martin and Gerdes*, 2007].

[30] We also adjusted the KPP background vertical diffusivity and two salt plume parameters. *Zhang and Steele* [2007] and *Nguyen et al.* [2009] discussed the importance of adjusting the vertical diffusivity in order to reduce numerical diffusion and to improve properties of the Atlantic and Pacific waters. In addition, *Nguyen et al.* [2009] showed that by including a subgrid-scale salt plume parameterization, a cold halocline could be realistically simulated in the Western Arctic Ocean.

[31] Lastly, we adjusted river runoff in order to bring the model freshwater budget closer to observations.

[32] Optimized parameter uncertainties can be estimated using equation (9) of *Menemenlis et al.* [2005a]. These uncertainties, however, depend on prior statistical assumptions, in particular on the implied data errors associated with the weights discussed in section 3.2. Option 2 of $\mathbf{W_y}$ yields the largest uncertainties (**A1** in Table 2) and is used here as a representative upper bound.

4. Results

[33] The optimization period covers 1992–2004. Simulation **A1** is integrated past the optimization period, i.e., to May 2009, in order to assess the model's ability to reproduce the sea ice and ocean conditions in recent years. Here we discuss the cost function reduction of **A1** relative to **A0** (section 4.1) and we provide a detailed assessment of simulation **A1**, including comparisons with observations outside the period of optimization (section 4.2).

4.1. Cost Function Reduction

[34] Cost functions are computed using three different weights, as discussed in section 3.2, and are referred to as J_1, J_2, and J_3. We optimize **A1** using J_2. In the following analyses, we also show costs J_1 and J_3 when they contribute additional insights. Figure 2 shows the total costs normalized by the cost of **A0**. The overall (ocean and sea ice) cost reduction in **A1** is 44% relative to **A0**. Four data sets for sea ice and two sets for the ocean are used to calculate the net cost. To assess sea ice mass balances, we use observations of extent, thickness, velocity, and fluxes. For the ocean, T/S profiles are used, which are metrics for water mass formation and evolution. Current meter measurements across the Fram Strait are used to evaluate the improvement in transports across this gateway.

4.1.1. Sea Ice Extent

[35] Sea ice extent costs J_{1-3} reduce by 3–17% in **A1** compared to **A0** (Figure 3b). A geographic breakdown

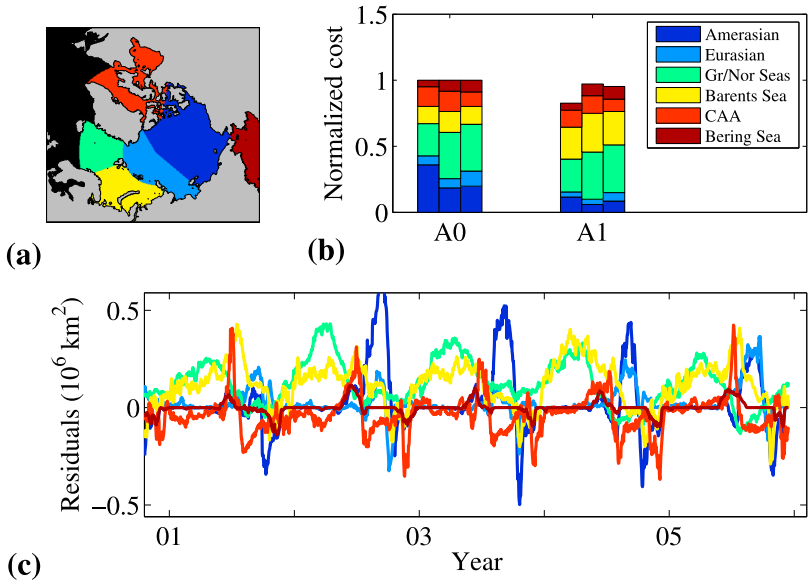

Figure 3. (a) Six geographic regions and (b) their corresponding sea ice extent cost. In Figure 3b, we show J_2 on the left, J_1 in the middle, and J_3 on the right. (c) A time series of sea ice extent residuals (**A1** minus data) shows that the contribution to the cost in Amerasian and Eurasian basins come from the mistiming of freezing in the late fall. High positive residuals in the Greenland/Norwegian (Gr/No) and Barents seas reflect the model tendency to produce too much sea ice in the marginal ice zones.

shows the largest reductions of 68% and 44% in the Amerasian and Eurasian basins. Costs increase in the marginal and seasonal ice zones such as in the Gr/No, Barents, and Bering seas (Figures 3b and 3c). In the Amerasian Basin and the CAA, a large fraction of the model-data difference is due to the model's mistiming of the onset of melting and freezing as compared to data (blue and red sharp extrema in Figure 3c). In the Gr/No and Barents Sea, the model produces more sea ice in both simulations compared to Special Sensor Microwave Imager (SSMI) data.

4.1.2. Sea Ice Thickness

[36] Sea ice thickness cost J_{1-3} reduce by 25–61% in **A1** compared to **A0** (Figure 4c). Regional reductions are ~62% in the Arctic Ocean and 41% in the Gr/No seas. **A0** has lower mean thickness than either **A1** or observations, even though the albedos are unrealistically high to compensate for deficiencies in the ERA40/ECMWF surface short-wave radiation (Figures 4a and 4b and Table 2). In **A1**, more realistic ice and snow albedos are obtained and sea ice thickness is closer to observations (Figure 4a). Improvements in thickness are also, in part, due to improved sea ice drifts [e.g., *Zhang and Rothrock*, 2003].

4.1.3. Sea Ice Velocity

[37] Sea ice velocity costs J_{1-3} reduce by 14–50% in **A1** relative to **A0** (Figure 5). There is no apparent temporal variation in the residuals. When costs in **A0** are partitioned into contributions from individual basins and seas and from the CAA, the Gr/No seas account for 68% of J_1 and 28% of J_2 (**A0**, Figure 5c). The spatial distribution of costs in **A1** is similar to **A0**, with model-data differences in the Gr/No seas accounting for 71% of J_1 and 43% of J_2 (Figure 5d).

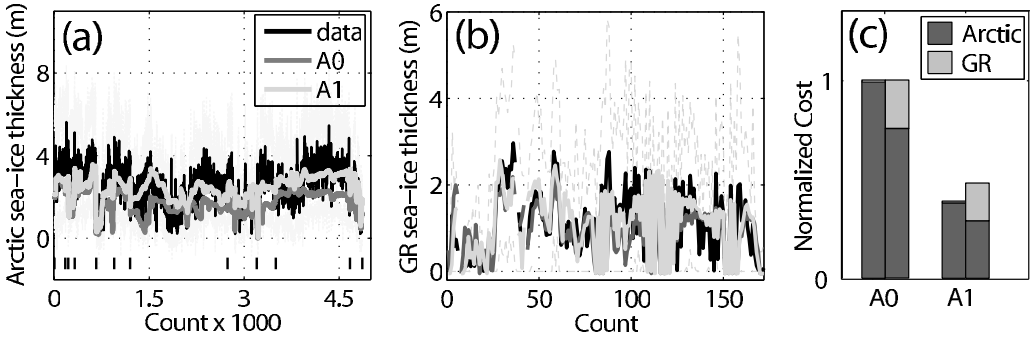

Figure 4. Sea ice thickness in the (a) Arctic Ocean and (b) Greenland/Norwegian seas and (c) cost reductions in **A1** compared to **A0**. The thin lines in Figures 4a and 4b show the standard deviation of ice drafts within each 20 km section. In Figure 4c, for each simulation, costs J_2 are shown on the left and J_1 on the right.

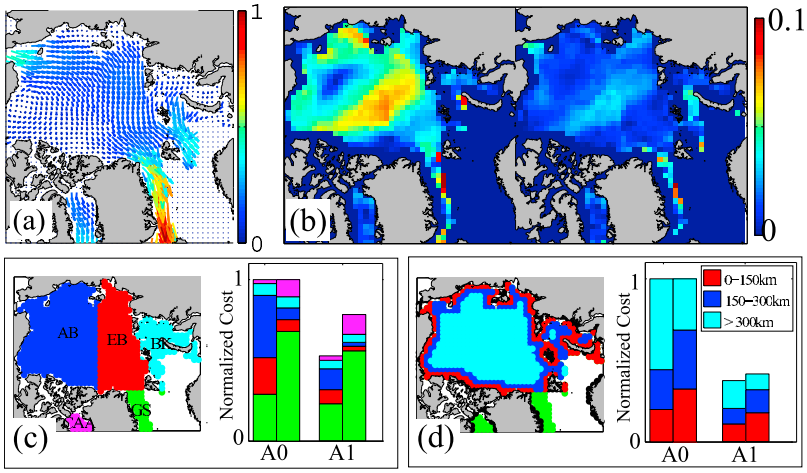

Figure 5. (a) Monthly sea ice velocity data for March 2002 in m/s, (b) model minus data velocity magnitude in m/s for (left) **A0** and (right) **A1**. Cost distributions based on (c) geographical regions and (d) distance from the coast are shown. Color scale in Figure 5a shows velocity magnitude in m/s. Costs at **A0**, **A1** are J_2 (left bars) and J_1 (right bars).

[38] Systematic spatial biases exist for sea ice velocity (Figure 5d). Within the Arctic Ocean, excluding the CAA and the Gr/No seas, model-data differences are higher along the coast. In **A0**, 55% of J_2 occurs within 150 km from the coast, and 94% of J_2 is within 300 km. A closer look at the velocity directions shows that, in addition to large speed differences, both simulations **A0** and **A1** have velocity directions approaching parallel to the coasts. In contrast, microwave data show sea ice flowing at angles 25–45° to the coast (not shown here). The large differences along the coast also reflect the model's inability to produce observed sea ice convergence/ridging. Overall, the reduction in sea ice velocity costs in **A1** is largely a result of optimizing the air/sea ice drag coefficients (Table 2).

4.1.4. Sea Ice Transports

[39] Monthly and annual sea ice transports across Fram Strait (FS) are significantly closer to observations in **A1** compared to **A0** (Figures 6a and 6b). Overall, both J_1 and J_2 reduce by ~58% (Figure 6c). Individual reductions of cost are 79% and 45% for FSa and FSb, respectively (see *Kwok et al.* [2004] for locations of FSa and FSb). Similar to sea ice velocity, improvements in transports mostly come from optimizing the ice-air drag coefficient.

4.1.5. Hydrography

[40] The overall hydrographic cost reductions are 60% for J_1 (not shown) and 54% for J_2 (Figure 7). A breakdown of costs shows a reduction in J_2 of 83% when compared to BGEP data (2003–2004) and a reduction of 54% when compared to SCICEX data (1992–2000, Figure 7). The largest decrease in J_2 comes from improvements in the cold halocline representation in the Western Arctic at depth 50–250 m and, to a lesser extent, improvements in Atlantic Water properties below 250 m (Figure 8). Improvements in water mass productions are a result of using the salt plume parameterization in combination a low KPP background diffusivity [*Nguyen et al.*, 2009]. Curvatures associated with the summer and winter Pacific Water at S ~ 28–34 and at T < 0°C in the T/S diagram are also more realistically reproduced in **A1** (Figure 8a). Vertical T/S profiles in MB, AB, and NB (see Figure 1 for locations) are similar and therefore we show vertical profiles for MB and T/S diagrams from AB and NB to aide visualizations in both depth space and T/S space (Figures 8b and 8c). In the Gr/No seas, both simulations produce thicker Atlantic Water than observed (Figure 8d) and as a result improvements in this region is negligible (Arctic/Subarctic Ocean Fluxes (ASOF) data, Figures 7 and 8d). The misrepresentation of the Atlantic

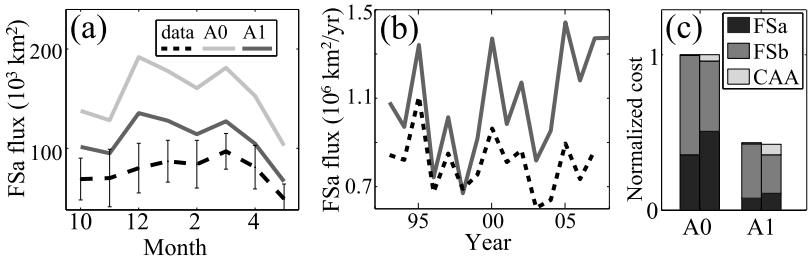

Figure 6. (a) Monthly and (b) annual sea ice area flux across Fram Strait and (c) cost reductions. In Figure 6c, total costs J_2 at **A0**, **A1** are shown on the left and J_1 are shown on the right. In Figure 6a, error bars show the 10 year data spread around the monthly mean fluxes. The annual flux for A0 is significantly higher than observation and is not shown in Figure 6b.

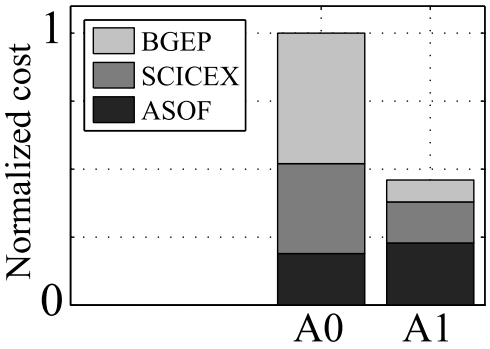

Figure 7. Hydrographic cost J_2 for **A0** and **A1**. The cost reduction is largest in the Amerasian Basin (BGEP data). In the Greenland/Norwegian seas, J_2 increases. Vertical T/S profiles in the Greenland and Norwegian seas, where J_2 increases, are shown in Figure 8d.

Water is a common problem in the AOMIP models [*Holloway et al.*, 2007].

[41] A possible mechanism contributing to a thicker Atlantic Water (AW) layer is the inability of our model to adequately represent restratification processes. *Boccaletti et al.* [2007] show that within a few days after a deep mixing event, instabilities develop that cause the convection region to restratify. In our model, this restratification process is not resolved.

4.2. Assessment of Simulation A1

4.2.1. Sea Ice

[42] In this section we assess **A1** relative to the mean, trend, and variability of sea ice conditions, with emphasis on recent years that are beyond the optimization period. With more realistic spatial sea ice thickness distribution, simulation **A1** can reproduce the extent minima in the summers of 2007 and 2008 (Figures 9a and 9b). For the 1992–2004 optimization period and for the 2005–2008 period, the mean model-data differences in September sea ice minimum are 4% and 10%, respectively (Figure 9c). *Parkinson and Cavalieri* [2008] report a negative trend of $-450 \pm 50 \times 10^3$ km^2/decade in observed sea ice extent from 1979–2006. For the period considered in this study, 1992–2008, the trend is more negative, approximately -680×10^3 km^2/yr for SSMI and -590×10^3 km^2/yr for **A1** (Figure 9d).

[43] For sea ice transport, **A1** overestimates the area flux across Fram Strait by ~20% in the annual mean and ~65% during the summer months when compared to estimates from *Kwok* [2009] (Figure 6b). This overestimation is in part because **A1** produces a wider sea ice extent across Fram Strait during the summer compared to observations and in part because we use only winter velocity to construct the cost function. Over the period 1992–2008, the mean annual, winter, and summer transports in **A1** are $109 \pm 24 \times 10^4$, $90 \pm 18 \times 10^4$, and $18 \pm 8 \times 10^4$ km^2, respectively. During the summer (June–September), **A1** yields maximum sea ice exports in years 2005 and 2007, consistent with *Kwok* [2009] but with a positive bias. In terms of interannual variability, annual transport peaks match the results of *Kwok* [2009], with maxima in 1995, 1997, 2000, 2002, 2005, and 2007 (Figure 6b). The **A1** simulation, however, has maximum area export in 2005, whereas observations show maximum export in 1995. *Kwok* [2009] concluded that even though there is an increase in velocity across FSa, there is no increase in outflow because of negative trends of sea ice concentration across this gate since 1979. In **A1** the reduction in ice concentration across Fram Strait for the 1992–2008 period is smaller than observed. As a result, due to

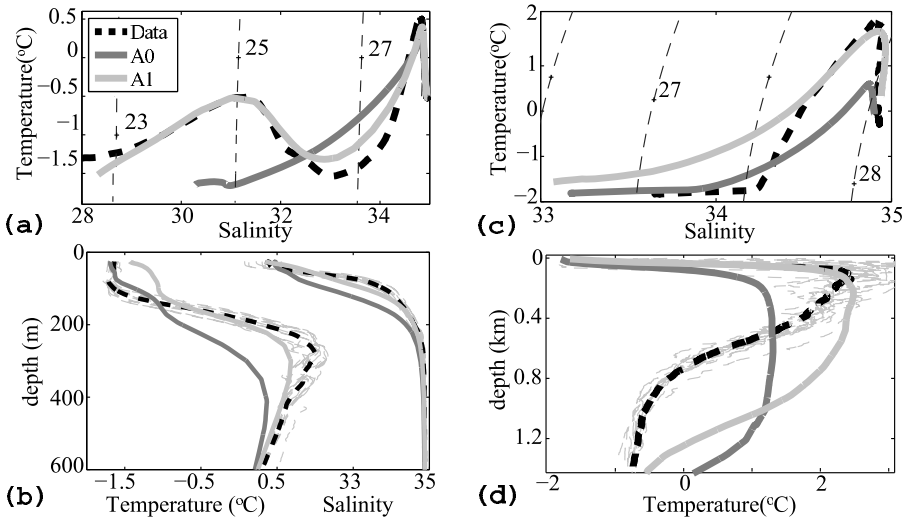

Figure 8. Hydrographic profiles for the (a) Canada Basin in August 2003, (b) Makarov Basin in October 2000, (c) Amundsen and Nansen basins in October 2000, and (d) Greenland/Norwegian seas in July 2001. In the Greenland/Norwegian seas, the Atlantic Water in the model (dark and light gray lines) is too thick compared to observation (dashed black lines). The thickening of the Atlantic Water is also observed in AOMIP models [*Holloway et al.*, 2007]. In the vertical temperature and salinity profiles in Figures 8b and 8d, actual CTD observations are shown as thin gray dashed lines with the data mean shown as thick black dashed lines. Dashed contours in T/S diagrams in Figures 8a and 8c are density anomalies σ.

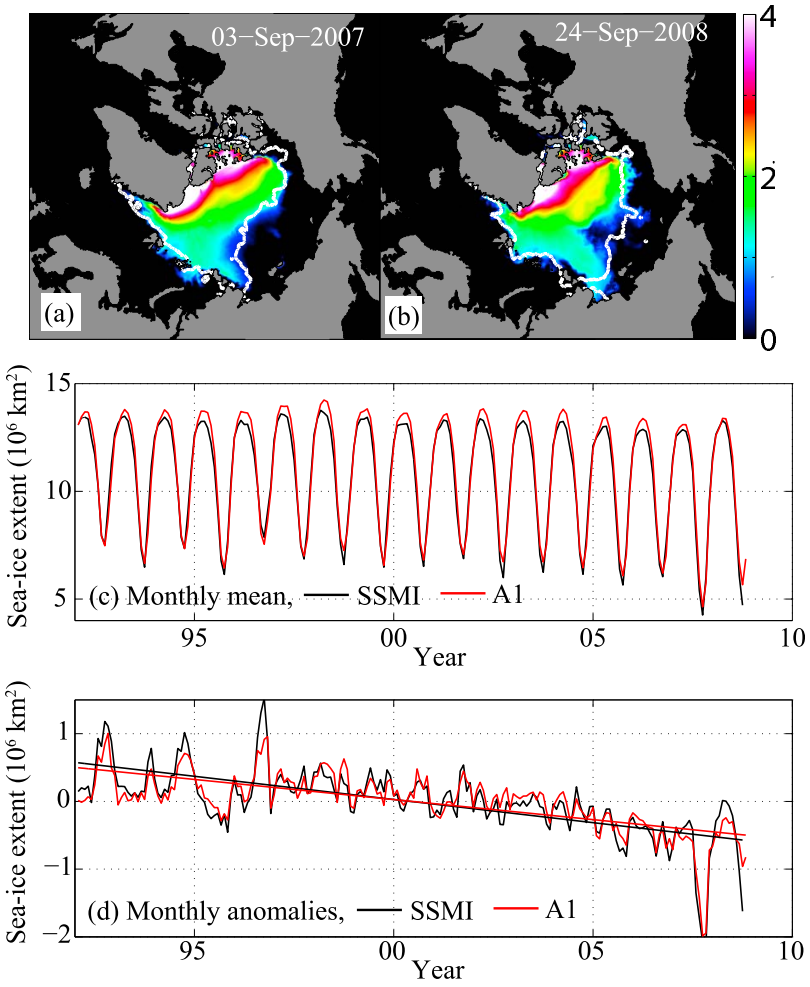

Figure 9. Sea ice minima for (a) 2007 and (b) 2008 and time series of monthly (c) mean sea ice extent and (d) anomalies for SSMI data and **A1**. Anomalies are calculated by subtracting monthly values from the 1992–2008 monthly means. Trends are -680×10^3 km^2/decade for SSMI and -590×10^3 km^2/decade for **A1**. For the 1992–2004 optimization period and 2005–2008 period, the mean model-data differences in September sea ice minimum are 4% and 10%, respectively.

increased velocity, the simulation has increased annual sea ice exports across this gate (Figure 6b).

[44] For sea ice thickness, the 2003–2008 **A1** estimates are consistent with Ice, Cloud, and land Elevation Satellite (ICESat)-derived estimates both for the basin-averaged thickness as well as for the thickness distribution (e.g., the mean and long tail of thick ice in Figure 10b). Spatial distributions of thickness are also consistent with ICESat data, e.g., the very thick ice (>5 m) North of Greenland and the CAA and thin ice near the Siberian Coast (Figure 10a). **A1** also reproduces the negative trend in mean November ice volume for the 2003–2007 period in the Arctic Ocean and Barents Sea; however the simulation underestimates the net volume loss, i.e., -3×10^3 km^3 for **A1** compared to -5×10^3 km^3 for ICESat (Figure 10c).

4.2.2. Atlantic Water

[45] The AW in **A1** is identified as the layer within $27.8 < \sigma < 33.0$ kg/m^3 (density anomaly relative to 1000 kg/m^3), which roughly corresponds to the layer of temperature T > 0°C. In addition, outside the Arctic Ocean, AW is also defined as having salinity S > 34.5. To determine the sense and strength of Atlantic Water circulation, we use the scalar field "topostrophy" τ as defined by *Holloway et al.* [2007]

$$\tau = \frac{(\mathbf{u} \times \nabla D) \cdot \hat{\mathbf{z}}}{|\mathbf{u}|^2 |\nabla D|^2}, \tag{8}$$

where $\mathbf{u}$ and ∇D are velocity and gradient of bathymetry D, respectively. In the Northern Hemisphere, τ is positive when the flow is cyclonic with shallow topography to the right (Figure 11).

[46] In the Gr/No and Barents seas, AW is close to the surface and can be traced in the top 270 m of the water column (Figure 11, left). In the Nansen and Amundsen basins, AW is present at depths below 50–70 m and flows in a cyclonic sense. In the Canada Basin, AW is at greater depth and its circulation is strongly cyclonic along the rim of the Arctic Ocean with $\tau \sim 0.4$–0.8 (Figure 11, right). Figure 12 shows the 16 year mean AW flow in the Arctic Ocean with strongest imports across FS and the St Ana

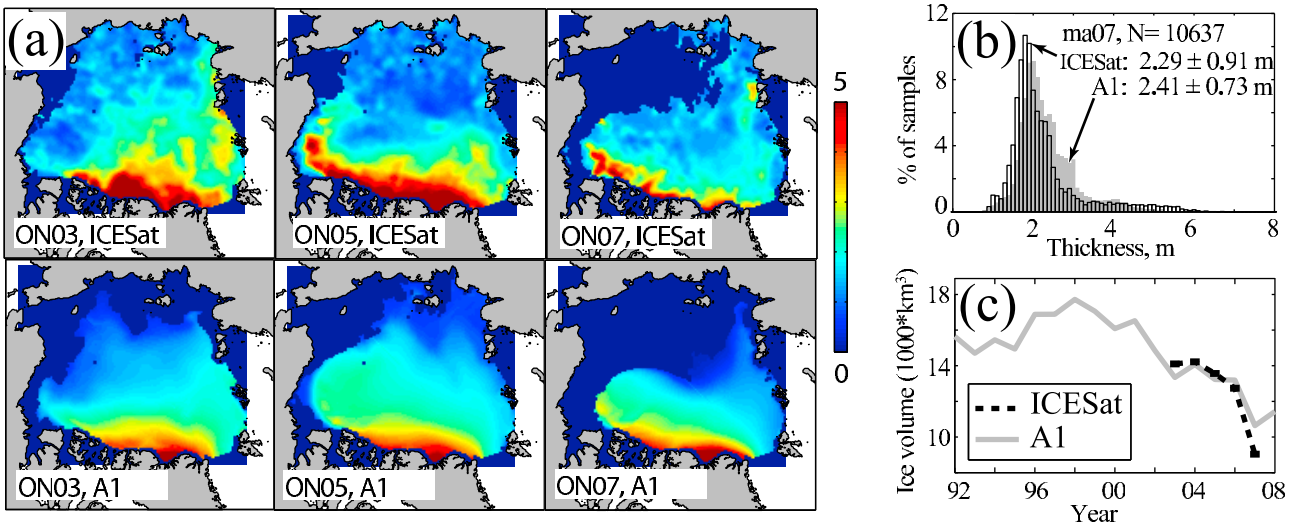

Figure 10. (a) Spatial distribution of sea ice thickness in October/November 2003 (ON03), 2005 (ON05), and 2007 (ON07) for (top) ICESat data and (bottom) **A1**. (b) Thickness distributions for March–April 2007 showing the long tail of thick ice in both ICESat data and **A1**. (c) Mean November sea ice volumes showing the negative trends from 2003–2007 in data and model. The net loss of ice volumes in November for the 2003–2007 period are 5×10^3 km^3 for ICESat and 3×10^3 km^3/yr for **A1**.

Trough (SA) into the Nansen Basin. Table 3 lists volume, heat, freshwater (relative to a salinity of 34.8), and salt transports across the major gates along the AW path. Transports here are calculated from the top of the AW to full depth of the water column. Salt transport in g/s is computed as volume flux (m^3/s) × salinity (g of salt/kg of salt water) × salt water density (kg/m^3), assuming a mean Atlantic salt water density of 1028 kg/m^3.

[47] The combined Kara and Barents seas are bounded by gates BA, SA, SF, and VS (Figure 13). The net inflows of volume, heat, and salt across these gates are 1.3 ± 0.4 Sv, 27 ± 11 TW, and 48.6 ± 16 Mg/s, respectively. The corresponding net outflows are 1.9 ± 0.3 Sv, 66 ± 9 Mg/s, and 4.6 ± 4.7 TW, respectively. The imbalance in heat transport is due to heat loss to the atmosphere and to sea ice melt. For freshwater, the annual mean runoff of 40.1 mSv from the Ob and Yenisey rivers contribute to a net flow of 20 ± 3 mSv of freshwater from the Barents and Kara seas into the Arctic Ocean.

[48] For the Arctic Ocean budget, AW volume and salt fluxes of 2.5 ± 0.3 Sv and 89 ± 11 Mg/s, respectively, through FS and 1.8 ± 0.3 Sv and 66 ± 9 Mg/s, respectively, through SA account for ~90% of the inflows (Figure 13). For heat fluxes, ~80% of the net input of 35 ± 5 TW is through FS and ~20% is through SA. As expected, the Arctic Ocean acts as a heat sink with ~30 TW of the input heat lost to sea ice melting and to the atmosphere and 3.5 ± 2 TW flowing out through FS. The addition of sea ice melt, river runoff (annual mean 39.5 mSv), and mixing with fresher Pacific Water likely accounts for the large freshwater pool with net outflow of 100 ± 20 mSv across the CAA, Nares Strait (NS), and FS.

[49] In term of circulation, AW enters the Arctic Ocean across FS and splits into two branches just inside this gate. The smaller branch of the two either recirculates and exits on the western side of FS or flows north across the Gakkel Ridge and reaches the Makarov Basin across gate A3 (Figure 12 and Table 3). The second branch flows east along the southern rim of Nansen Basin, merges with the inflow through SA, and continues eastward along the 500–2000 m isobaths in the Nansen and Amundsen basins (gate A1 in Table 3). At the southern end of the Lomonosov Ridge, the flow splits with ~50% flowing along the Lomonosov Ridge back out to Fram Strait and ~50% continuing along bathymetric contours near the Siberian Coast into the Canada Basin. Along the Canada Basin rim, AW flows beneath the lighter Pacific Water. Volume fluxes reduce from ~1.5 Sv at gates C1–CK to 0.5–1.0 Sv across gates C2–C5 (Figure 12).

[50] The net volume flux across FS of 1.4 ± 0.6 Sv is comparable with observations of 2–4 Sv [*Schauer and Fahrbach*, 2004]. The individual northward and southward flows, however, are lower than the observed values of 9 ± 2 Sv (inflow) and 13 ± 2 Sv (outflow). Consequently, the

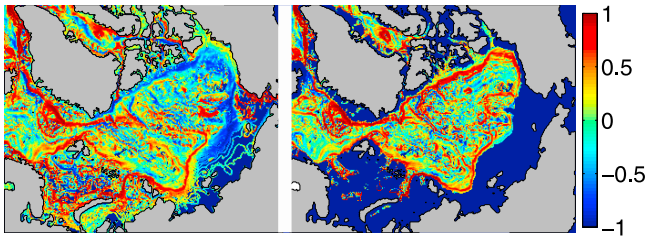

Figure 11. The 16 year mean topostrophy τ in (left) the top 270 m and (right) 270–3000 m for simulation **A1**. In Figure 11 (left), the Atlantic Water in the Eurasian Basin circulates in a cyclonic sense (positive τ), while the Pacific Water in the Beaufort Gyre flows in an anticyclonic sense (negative τ). At depth below 270 m, Atlantic Water flows in a cyclonic sense along the rim of the Arctic Ocean in both the Eurasian and Amerasian basins.

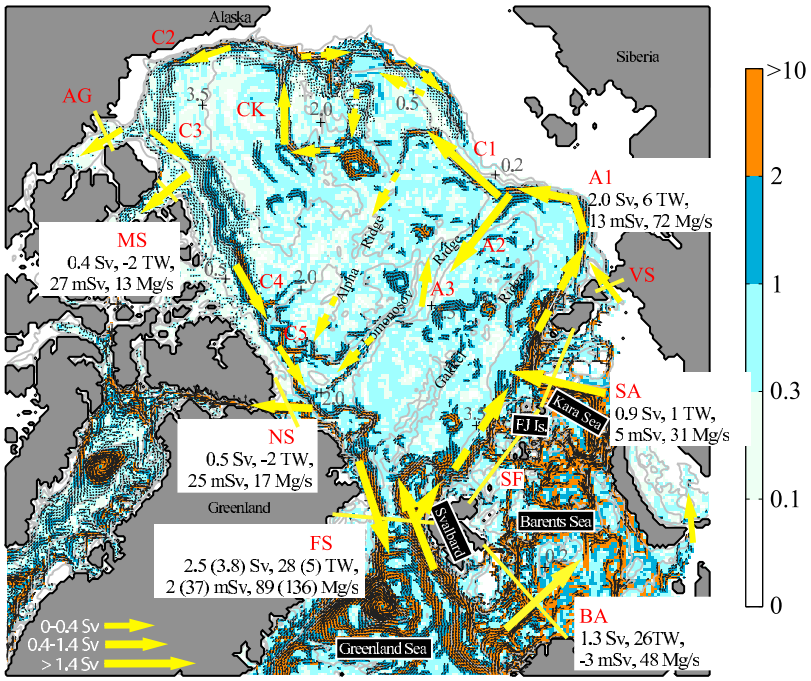

Figure 12. The 16 year mean Atlantic Water pathways in simulation **A1**. Background color shows the velocity magnitude |**u**| in cm/s. Only velocity vectors with |**u**| > 1 cm/s are shown for clarity. One exception is in the Canada Basin where velocity vectors with |**u**| < 1 cm/s are also shown. Large yellow solid arrows show total Atlantic Water transports with the provided scale in the legend. Large dashed yellow arrows are inferred transports based on current strengths. Estimates of transports into the Arctic Ocean through FS and SA are lower than those from observations [*Schauer and Fahrbach*, 2004] and high-resolution modeled climatology [*Maslowski et al.*, 2004]. The Atlantic Water cyclonic flow patterns are consistent with previous model results [*Maslowski et al.*, 2004; *Rudels et al.*, 2004; *Karcher et al.*, 2007]. Net transports are shown across all important gates with the exception of the Fram Strait. At Fram Strait, inflows and outflows are shown in pairs with outflows shown in parentheses. The strong velocity feature just north of the Chukchi Cap follows the model bathymetry. We currently do not have data in this area to verify the presence and strength of this flow (R. Woodgate, personal communication, 2010).

Table 3. Transports in Simulation **A1** Along the Atlantic Water Pathways in the Arctic Ocean and Barents and Kara Seas[a]

Gate	V_i (Sv)	V_o (Sv)	T_i (TW)	T_o (TW)	FW_i (mSv)	FW_o (mSv)	S_i (Mg/s)	S_o (Mg/s)
BA	2.1 (0.4)	0.8 (0.2)	35.7 (10.8)	9.4 (2.7)	2 (1)	5 (2)	76.0 (16.0)	27.4 (6.6)
SA	2.1 (0.3)	0.4 (0.1)	7.8 (4.7)	4.0 (0.9)	12 (2)	1 (1)	75.4 (9.7)	15.9 (3.3)
SF	0.2 (0.1)	0.1 (0.1)	1.6 (0.7)	1.1 (0.3)	1 (2)	1 (1)	8.4 (2.5)	4.7 (y2.2)
VS	0.1 (0.0)	0.0 (0.0)	0.0 (0.0)	0.3 (0.1)	6 (3)	0 (0)	2.7 (1.2)	0.0 (0.1)
FS	2.5 (0.3)	3.8 (0.6)	27.6 (4.2)	4.9 (1.6)	2 (2)	37 (19)	89.1 (11.7)	135.6 (20.0)
NS	0.0 (0.0)	0.5 (0.1)	2.1 (0.7)	0.1 (0.1)	0 (2)	25 (5)	0.3 (0.6)	17.4 (3.7)
AG	0.1 (0.1)	0.1 (0.1)	0.1 (0.2)	0.1 (0.1)	5 (6)	3 (4)	1.7 (0.9)	1.7 (0.0)
MS	0.0 (0.0)	0.4 (0.1)	1.9 (0.5)	0.0 (0.1)	0 (2)	28 (6)	0.8 (0.9)	13.9 (3.0)
CAA	0.0 (0.0)	0.2 (0.1)	0.8 (0.3)	0.0 (0.0)	0 (0)	10 (3)	0.1 (0.3)	5.9 (1.7)
A1	2.1 (0.9)	0.1 (0.2)	6.5 (4.2)	0.9 (1.2)	13 (4)	0 (1)	74.3 (30.5)	1.9 (7.6)
A2	0.8 (0.8)	0.4 (0.5)	1.2 (0.6)	2.5 (1.7)	0 (1)	5 (2)	29.8 (29.2)	14.3 (16.7)
A3	0.5 (0.5)	0.8 (0.7)	3.2 (1.8)	0.8 (2.1)	1 (1)	20 (9)	18.2 (16.4)	29.3 (26.1)
C1	2.4 (0.3)	0.2 (0.3)	5.3 (3.4)	1.1 (1.0)	11 (5)	5 (5)	85.5 (11.6)	6.1 (9.0)
CK	2.7 (1.2)	0.6 (0.3)	3.0 (0.5)	3.0 (1.5)	11 (9)	33 (6)	97.2 (43.4)	18.4 (8.6)
C2	1.7 (0.7)	0.9 (0.3)	4.2 (0.8)	1.0 (0.3)	1 (3)	69 (22)	60.5 (23.6)	31.4 (11.5)
C3	1.1 (0.6)	0.4 (0.2)	2.5 (0.7)	0.6 (0.2)	1 (1)	36 (13)	40.5 (21.1)	13.5 (8.1)
C4	2.5 (1.2)	0.5 (0.2)	3.5 (1.0)	1.6 (0.6)	5 (3)	29 (9)	88.7 (41.7)	15.1 (7.2)
C5	0.6 (0.2)	0.8 (0.1)	3.1 (0.5)	0.4 (0.4)	2 (10)	31 (0)	22.8 (8.7)	25.9 (3.3)

[a]Gate locations are shown in Figures 1 and 12. Gates BA through VS are used for Barents and Kara seas budgets, and gates SA through CAA are used for Arctic Ocean budgets. Gate CAA is defined by *Kwok* [2006] and its location is between gates MS and NS in Figure 1.

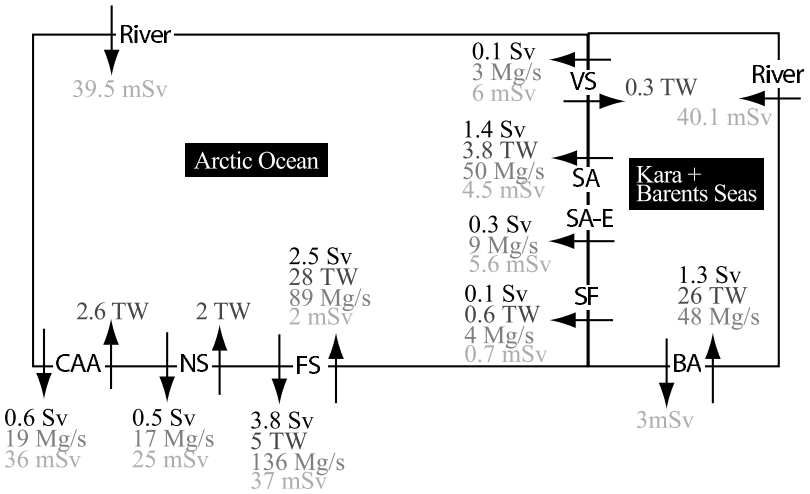

Figure 13. Atlantic Water freshwater budgets in the Arctic Ocean and Kara/Barents seas in simulation **A1**. In the Kara/Barents seas, ~80% of the incoming heat through the Barents Sea opening (gate BA) is lost to the atmosphere and sea ice melt, and a net 20 ± 3 mSv of freshwater is produced here through sea ice melt and river runoff. In the Arctic Ocean, ~84% of the input heat is lost to the atmosphere and sea ice melt. In addition, the Arctic Ocean is a source of freshwater with ~80% of its outflow (~100 mSv) coming from river runoff, precipitation, and mixing with less salty Pacific Water (see also Table 5).

heat flux into the Arctic Ocean across FS (28 ± 4 TW) is lower than the observed value of 28–46 TW. A closer look at T/S diagrams shows that the Atlantic Water in the Gr/No seas is thicker and extends deeper compared to climatology (Figure 8d). This misrepresentation of AW is also present in the AOMIP simulations and is identified as one of the major deficiencies in current generation coupled ocean and sea ice models [*Holloway et al.*, 2007].

[51] Despite weaker than observed flows across Fram Strait, the strength of the cyclonic flow inside the Eurasian Basin, as measured by positive topostrophy (Figure 11), is stronger than flows in all AOMIP simulations that do not include a subgrid-scale parameterization to force flow along local topographic contours [*Holloway and Wang*, 2009]. The 15 year mean normalized τ for the upper 1500 m are 0.68 ± 0.19, 0.12 ± 0.32, 0.52 ± 0.08, and 0.58 ± 0.13 for the Eurasian, Amerasian, Barents and Kara seas, and Gr/No seas, respectively. The low τ in the Amerasian Basin is due to the inclusion of the upper ocean where the Beaufort Gyre dominates. For depth 150–1500 m in the Amerasian Basin, τ = 0.53 ± 0.41. These highly positive τ values in the entire Arctic Ocean indicate that cyclonic flow is prominent and that anticyclonic atmospheric circulation over the Beaufort Sea acts to weaken the AW flow below 300 m but does not reverse it.

4.2.3. Pacific Water

[52] Pacific Water (PW) in **A1** enters the Canada Basin through Bering Strait (BS) and can be traced in the upper 270 m by the strongly negative topostrophy (anticyclonic flows, Figure 11, left). After crossing Chukchi Sea where nearly 50% of the heat input is lost, passive tracers show that PW follows roughly the bathymetric contours into the Arctic Ocean along the Barrow (BC1), Central (CC), Herald Canyons (HC), and Long Strait (LS) (Figure 14). Transports across the gates shown in Figure 14 and comparisons with previously published results are summarized in Table 4. At BS, the net imports of volume, heat, and freshwater are 0.86 ± 0.03 Sv, 9.34 ± 0.34 TW, and 70 ± 2.6 mSv, respectively. These transports are consistent with observed values of ~0.8 Sv, 4.12–9.19 TW, and 41–67 mSv, respectively [*Woodgate et al.*, 2005]. The fractional transports across BC1, CC, HC, and LS are 30%, 40%, 20%, and 10%, respectively (Table 4). For comparison, estimates from a Chukchi Sea high-resolution numerical model [*Spall*, 2007] and from mooring observations [*Woodgate et al.*, 2006] across BC1, CC, and HC are ~25%, ~25%, and ~50%, respectively, of the net ~0.8 Sv inflow through BS. Residence time of PW in the Chukchi Sea is ~1 year.

[53] At the northern end of the Chukchi Sea, flow across gate BC1 continues downstream to gate BC2. At BC2 80–90% of this flow merges with the flow through CC and becomes part of the anticyclonic Beaufort Gyre circulation. A small fraction of the flow (0.05 ± 0.02 Sv) at gate BC2 continues eastward as the rim current along the coast of Alaska. Transit time between gates CC1 and McClure Strait (MS) along the Beaufort Gyre circulation is 5–6 years. Downstream of HC, the flow splits into two branches. One branch merges with water from CC and becomes part of the anticyclonic Beaufort Gyre circulation. The second branch flows westward along the 500 m isobath near the East Siberian Sea, then flows into the Makarov Basin, crosses the Lomonosov Ridge, and reaches NS and FS. The transit time from BS to NS or from BS to FS is ~10 years. The largest export of PW at the CAA comes from water along path A–B and exits through McClure Strait (0.34 ± 0.09 Sv, Table 4). Export at Amundsen Gulf (AG) comes from path A–B and from the rim current but is much weaker (0.05 ± 0.02 Sv). The net exports are 0.55 ± 0.12, 0.32 ± 0.08, and 0.41 ± 0.17 Sv across the entire Canadian Arctic Archipelago (gates CAA, AG, and MS), the Nares Strait, and the Fram Strait, respectively.

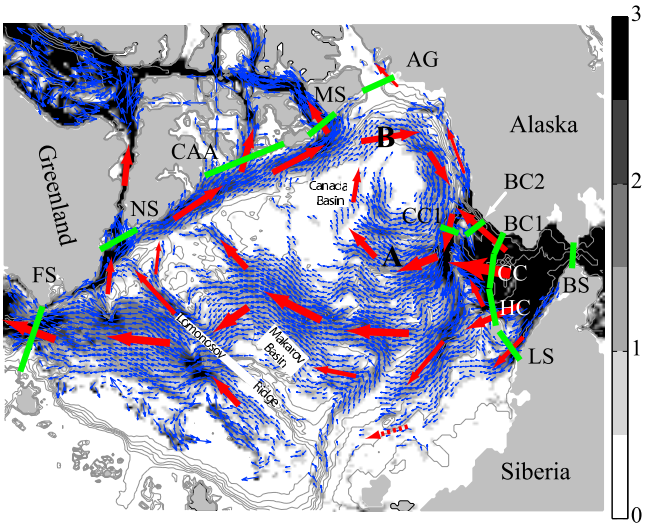

Figure 14. Simulation **A1** 12 year mean flow (1995–2006) of Pacific Water in the upper 100 m using passive tracers. The flow magnitude in cm/s is indicated by the gray-scale background. White areas indicate regions where $|\mathbf{u}| < 0.5$ cm/s, black areas indicate regions where $|\mathbf{u}| \geq 2.5$ cm/s, and gray areas with blue arrows indicate regions where $0.5 \leq |\mathbf{u}| < 2.5$ cm/s. Contours show the bathymetry. Warm Pacific Water flows northward across BS into the Chukchi Sea, then enters the Arctic Ocean interior through four branches: Long Strait (LS), Herald Canyon (HC), Central Canyon (CC), and Barrow Canyon (BC1). At downstream of Barrow Canyon (gate BC2), 80–90% of the flow is "peeled" off and merges with that of the Beaufort Gyre circulation. Approximately 10% of the water reaching BC2 flows eastward along the Alaskan Coast. Pacific Water, which crosses HC and CC, becomes part of the Beaufort Gyre circulation and eventually reaches McClure Strait (MS) after ~5 years. Some of the water flows along the Transarctic Drift before reaching the coast of Greenland and flowing out to Fram and Nares straits. Transit time of Pacific Water between Bering Strait and Fram Strait is ~10 years.

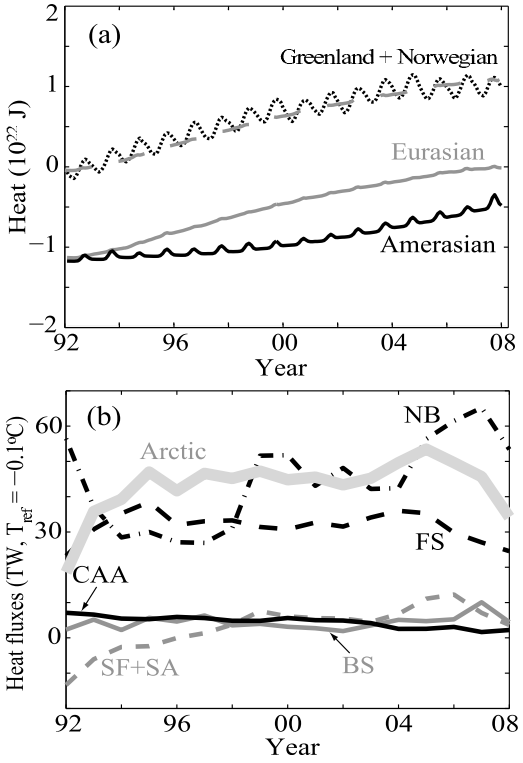

Figure 15. (a) Simulation **A1** heat content in the Amerasian Basin (solid black), Eurasian Basin (solid gray), and Greenland/Norwegian seas (dotted black). The Eurasian Basin's heat content with a vertical shift is shown in dashed gray to highlight similar trends. (b) Heat fluxes into the Barents Sea (gate BA, dash-dotted) and into the Arctic (thick gray) through the CAA (solid black), BS (solid gray), FS (dashed black), and SF + SA (dashed gray). See section 4.2.4 for discussion.

[54] Overall, net imports of volume, freshwater, and salt transports of 0.98 ± 0.03 Sv, 80 ± 2.2 mSv, and 31 ± 0.8 Mg/s across the four Chukchi Sea gates (BC, CC, HC, and LS) are balanced by net exports of 1.28 ± 0.22 Sv, 85 ± 11 mSv, and 40 ± 7 Mg/s through the CAA, Nares Strait,

Table 4. Transports of Pacific Water in the Arctic Ocean for Simulation **A1**[a]

Gate	V (Sv)	*Woodgate et al.* [2005]	*Spall* [2007]	T[b] (TW)	FW (mSV)	S (Mg/s)
BS	0.86 ± 0.03	0.8	0.8 ± 0.2	9.34 ± 0.34[c]	69.7 ± 2.6[d]	28.28 ± 1.05
BC1	0.29 ± 0.02	0.2	0.16 ± 0.07	2.28 ± 0.13	26.5 ± 1.5	9.21 ± 0.53
CC	0.39 ± 0.01	0.2		1.82 ± 0.04	30.6 ± 0.6	12.44 ± 0.25
HC	0.19 ± 0.01	0.4	0.28 ± 0.12	0.75 ± 0.01	14.0 ± 0.3	5.78 ± 0.08
LS	0.11 ± 0.02		0.18 ± 0.12	0.40 ± 0.06	9.3 ± 1.4	3.37 ± 0.48
BC2	0.26 ± 0.02			1.18 ± 0.10	24.0 ± 2.1	8.41 ± 0.71
CC1	0.47 ± 0.05			1.75 ± 0.20	39.4 ± 4.6	16.50 ± 1.73
MS	0.34 ± 0.09			0.82 ± 0.20	25.8 ± 5.4	10.79 ± 2.74
NS	0.32 ± 0.08			0.65 ± 0.20	21.2 ± 3.3	10.16 ± 2.48
FS	0.41 ± 0.17			0.61 ± 0.35	24.3 ± 7.6	13.72 ± 5.90
AG	0.05 ± 0.02			0.20 ± 0.12	3.3 ± 1.8	1.26 ± 0.73
CAA	0.16 ± 0.08			0.28 ± 0.15	10.3 ± 5.2	4.36 ± 2.29

[a]See Figure 14 for gate locations.
[b]$T_{ref} = -1.9$°C.
[c]Compared to 4.12–9.19 TW from *Woodgate et al.* [2005].
[d]Compared to 41–67 mSv from *Woodgate et al.* [2005].

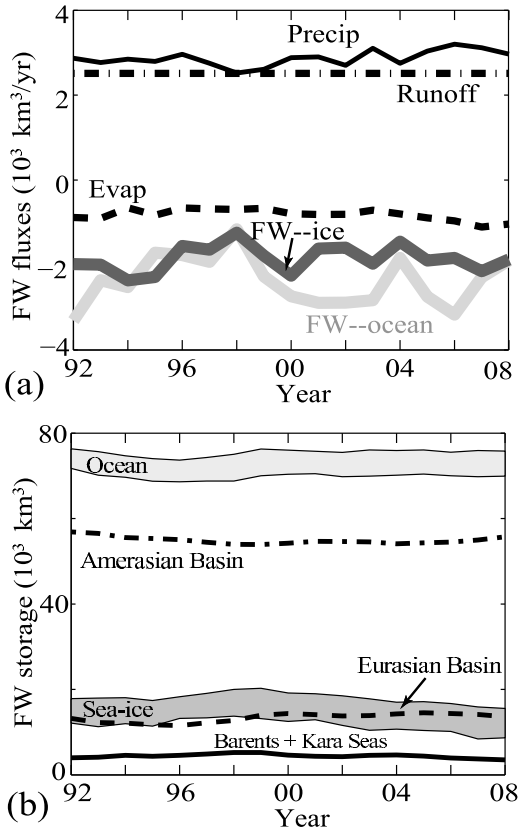

Figure 16. (a) Freshwater fluxes and (b) storage in the Arctic Ocean for simulation **A1**. See Table 5 for the freshwater budget and section 4.2.4 for discussion.

and Fram Strait. Here, a salt water density of 1025 kg/m^3 is used to calculate salt transport.

4.2.4. Freshwater and Heat Budgets

[55] The heat content in simulation **A1** in the Amerasian and Eurasian basins are close to the Environmental Working Group climatological range of −0.7 to −0.9 × 10^{22} J for the 1990s (Figure 15) [see *Holloway et al.*, 2007, Figure 3]. A drift of ~4.3 × 10^{20} J/decade in the Amerasian Basin is similar to that in AOMIP models [*Holloway et al.*, 2007]. The largest increase in heat storage occurred after year 2000 and can be partially explained for by the increase of 1.6 × 10^{20} J/decade in heat flux across Bering Strait (gate BS in Figure 15b). This simulated heat flux trend is lower than the observed rate of ~6 × 10^{20} J/decade between 2001 and 2004 [*Woodgate et al.*, 2006].

[56] In the Eurasian Basin, a drift of ~7.7 × 10^{20} J/decade is on the high end of the range of drifts seen in AOMIP models [*Holloway et al.*, 2007]. A similar positive trend exists in the Gr/No seas region (Figure 15a). *Dmitrenko et al.* [2008] and *Schauer and Fahrbach* [2004] have reported an increase in the core AW temperature since the late 1990s in the Gr/No seas and in the Eurasian Basin. Specifically, *Dmitrenko et al.* [2008] observed in mooring data a large jump in AW core temperature of ~0.8°C. When the observed volume flux of ~6 Sv across FS is used, the heat increase is ~20 TW, which is consistent with the observed increase of 23 TW for the 1997–1999 period [*Schauer and Fahrbach*, 2004]. In simulation **A1**, however, two pulses of heat flux increase are seen at gate BA into the Barents Sea and there is no apparent increase across Fram Strait (Figure 15b). Overall, a heat flux rate of ~9 × 10^{20} J/decade from the Barents and Kara seas into the Eurasian Basin across gates SF and SA explains for the heat storage trend in the Eurasian Basin.

[57] In the Amerasian basin, average incoming heat from the Bering Sea (~5 TW in Figure 15b) is comparable with values of 4.1–9.2 estimated by *Woodgate et al.* [2006] for the years 1998–2004. Overall, the net heat flux into the Arctic Ocean (sum of fluxes across gates CAA, FS, BS, SF, and SA) is dominated by values across FS and remains approximately constant (Figure 15b).

[58] Figure 16 shows freshwater fluxes and storage in the Arctic Ocean. To be consistent with *Serreze et al.* [2006] freshwater estimates, Arctic Ocean in this section includes the Barents and Kara seas. Freshwater content (FWC) in the Amerasian Basin is 55 ± 1 × 10^3 km^3 and is higher than climatological values of 34 ± 2 × 10^3 km^3 [*Holloway et al.*, 2007, Figure 16c]. Inputs into the Amerasian Basin include inflows through BS (80 mSv, 2525 km^3/yr, Tables 4 and 5), runoffs from the MacKenzie and Kolyma Rivers (~9 mSv), and transports of freshwater along the AW path. Monthly mean river runoff is based on the ARDB and was prepared by P. Winsor (personal communication, 2007). In the Eurasian Basin, FWC of 13 ± 1 × 10^3 km^3 is higher than the climatological value of 0 ± 3 × 10^3 km^3 [*Holloway et al.*, 2007, Figure 16c]. For comparison, AOMIP results yield

Table 5. Freshwater Budgets From **A1** and *Serreze et al.* [2006][a]

	Model	*Serreze et al.* [2006]	Comment
Area	10.01 × 10^6 km^2	9.58 × 10^6 km^2	
Storage (km^3)			
Ocean	72,500 ± 2100	74,000 ± 7400	
Sea ice	15,100 ± 2600[b]	~10,000	
Fluxes (km^3/yr)			
Precipitation	2900	3300 ± 680	
Evaporation	−780	−1300 ± 710 (−680[c])	
Runoff	2500	3200	
BS_w	2100	2500	Bering Strait
BS_i	60	-	
FS_w	−1500	−2660[d]	Fram Strait
FS_i	−1900	−2300	
CAA_w	−2330	−3200 ± 320	Canadian Arctic Archipelago
CAA_i	−20	−160	
BA_w	−660	−90	Norwegian to Barents Sea
BA_i	−220	-	
Total			
In	7560	9000	
Out	−7410	−9710 (−9090[c])	
Net	+150	−710	
Percentage	2%	8%	

[a]Freshwater content is calculated as $FWC = (S - S_{ref})/S_{ref} * Vol$, where $S_{ref} = 34.8$ is the reference salinity and *Vol* is the volume of water in the Arctic. Negative contributions are included in flux and excluded in storage calculations.

[b]AOMIP hindcast is 11,000–25,000 km^3 [*Gerdes and Köberle*, 2007].

[c]Value if evaporation is masked out by sea ice.

[d]Flux includes contributions of positive surface freshwater near surface and negative returned flow at depth and the West Spitzbergen current.

wide ranges of -10×10^3 to 30×10^3 km^3 for the Amerasian Basin and 10×10^3 to 100×10^3 km^3 for the Eurasian Basin.

[59] A freshwater budget and comparison with *Serreze et al.* [2006] (hereafter SR06) are shown in Table 5. For atmospheric input, the largest difference is in the mean evaporation, 780 km^3/yr in our model versus 1300 km^3/yr in SR06. This difference originates from the model not taking into account sublimation over sea ice. As a consequence of having less evaporation, simulation **A1** requires less river runoff inputs than the observed values (Table 5). For sea ice fluxes, SR06 used the higher estimates of sea ice exports from *Vinje et al.* [1998] instead of those from *Kwok et al.* [2004]. As a result, because we used *Kwok et al.* [2004] sea ice export to optimize for the air/sea ice drag coefficients, our sea ice FW contributions are consistently smaller than corresponding values from SR06. For oceanic freshwater fluxes, the low export across Fram Strait is due to lower than observed volume transports (see section 4.2.2). Across gate BA (see Figure 1 for location), our estimates of freshwater fluxes from Barents Sea into Norwegian Sea are higher than the net outflow of −90 km^3/yr in SR06 (positive Norwegian Coastal Current (+250 km^3/yr) being balanced out by negative inflow of deep AW (−340 km^3/yr)). In term of storage, the contribution from sea ice of 15100 ± 2600 km^3 is slightly higher than the approximate number used in SR06. Overall, the net inflow of our optimized simulation is ~85% of that in SR06. The simulation's outflow balances the input and closes the FW budget to within 2% (total percentage in Table 5).

5. Concluding Remarks

[60] An optimized ocean and sea ice solution is obtained for the Arctic Ocean using a Green's function approach for the 1992–2004 period. The solution, based on the adjustments of 16 ocean and sea ice parameters (Table 2), shows significant improvements compared to the baseline with an overall cost reduction of 45%.

[61] For surface boundary conditions, the change from ERA40 to JRA25 had a significant positive effect on the model solution. Specifically, the JRA25 fields with more realistic downward radiation [*Onogi et al.*, 2007] result in improved sea ice thickness and extent, and in river runoffs that are closer to the *Serreze et al.* [2006] estimates (Figures 4–9 and Table 5). Of note is that the optimized albedos are closer to the observed values when JRA25 forcing is used (Table 2).

[62] In the ocean, changing the KPP background diffusivity from 10^{-5} m^2/s to 5.4×10^{-7} m^2/s in combination with the salt plume parameterization of *Nguyen et al.* [2009] maintains a vertical T/S stratification that is much closer to observations (Figure 8).

[63] For 2005–2008, the quality of the simulation remains comparable to that during the 1992–2004 optimization period. The simulation continues to reproduce the observed September monthly mean sea ice extent minima to within ~10% (Figure 9). In addition, the observed 2003–2007 ICESat ice volume loss is reproduced in the simulation (Figure 10c). For the entire 1992–2008 period (i.e., including both the optimization period and the 2005–2008 extension), the loss of 590×10^3 km^2/decade in sea ice extent is consistent with SSMI analysis (Figure 9d).

[64] Decadal circulation and transport of Atlantic and Pacific waters are consistent with other model estimates and with observations (Figures 11–14 and Table 4). The circulation of the Atlantic Water in the 16 year simulation is cyclonic with mean topostrophy 0.4–0.8. Net northward and southward fluxes across Fram Strait are 2.1 Sv and 0.8 Sv for volume and 36 TW and 9 TW for heat. These simulated fluxes across Fram Strait are lower than observations. Approximately 80% of the heat input from the Atlantic Water is lost to sea ice melt and to the atmosphere. The volume, heat, and freshwater transports of Pacific Water across Bering Strait are 0.86 ± 0.03 Sv, 9.34 ± 0.34 TW, and 70 ± 2.6 mSv, consistent with observations (Figure 14, Table 4). Pacific Water crosses the Chukchi Sea where it loses ~50% of its heat before reaching the interior of the Arctic Ocean through the Barrow, Central, and Herald Canyons. The largest export of Pacific Water is through the Canadian Arctic Archipelago and the Nares Strait. The transit time from the Bering Strait to the Canadian Arctic Archipelago is ~5 years and the transit times from the Bering Strait to the Nares and Fram straits are ~10 years.

[65] Residual model-data differences after optimization persist and highlight deficiencies in the model equations and subgrid-scale parameterizations. Here, these residual differences include misrepresentation of Atlantic Water (Figure 8d), low transports across Fram Strait (Figure 12), and lack of sea ice deformation mechanisms (Figure 5). Understanding the causes for these residuals is a way toward improved representation of ice-ocean processes in climate models. For example, the misrepresentation of Atlantic Water might be improved either by increased resolution or by improved representation of subgrid-scale restratification processes [e.g., *Fox-Kemper et al.*, 2008]. Although adjoint method studies, such as those of *Kauker et al.* [2009], *Fenty* [2010], and *Heimbach et al.* [2010] provide a more complete description of model parameter sensitivities, this paper demonstrates that Green's functions are a simple but powerful tool for analyzing and optimizing a coupled ocean and sea ice simulation.

[66] **Acknowledgments.** Sea ice draft data were downloaded from the National Snow and Ice Data Center (NSIDC). This work is funded by the ECCO2 project, a contribution to the NASA Modeling Analysis and Prediction (MAP) program. We gratefully acknowledge computational resources and support from the NASA Advanced Supercomputing (NAS) Division and from the JPL Supercomputing and Visualization Facility (SVF).

References

Adcroft, A., and J.-M. Campin (2004), Rescaled height coordinates for accurate representation of free-surface flows in ocean circulation models, *Ocean Modell.*, *7*, 269–284.

Adcroft, A., C. Hill, and J. Marshall (1997), The representation of topography by shaved cells in a height coordinate model, *Mon. Weather Rev.*, *125*, 2293–2315.

Allan, R., M. Ringer, J. Pamment, and A. Slingo (2004), Simulation of the Earth's radiation budget by the European Centre for Medium-Range Weather Forecasts 40-year reanalysis (ERA40), *J. Geophys. Res.*, *109*, D18107, doi:10.1029/2004JD004816.

Antonov, J. I., R. A. Locarnini, T. P. Boyer, A. V. Mishonov, and H. E. Garcia (2006), *World Ocean Atlas* 2005, vol. 2, *Salinity*, *NOAA Atlas NESDIS*, vol. 62, edited by S. Levitus, 182 pp., NOAA, Silver Spring, Md.

Boccaletti, G., R. Ferrari, and B. Fox-Kemper (2007), Mixed layer instabilities and restratification, *J. Phys. Oceanogr.*, *37*, 2228–2250, doi:10.1175/JPO3101.1.

Boyd, T., M. Moustafa, and M. Steele (1998), Submarine-based hydrographic observations of the Arctic Ocean, *Data Rep. 165*, Oregon State Univ., Corvallis, Oreg.

Briegleb, B., C. Bitz, E. Hunke, W. Lipscomb, M. Holland, J. Schramm, and R. Moritz (2004), Scientific description of the sea ice component in the Community Climate System Model, version three, *Technical Note NCAR/TN-463+STR*, 70 pp., Natl. Cent. for Atmos. Res., Boulder, Colo.

Comiso, J., D. Cavalieri, C. Parkinson, and P. Gloersen (1997), Passive microwave algorithms for sea ice concentration: A comparison of two techniques, *Remote Sens. Enrivon.*, *60*, 357–384.

Condron, A., P. Winsor, C. Hill, and D. Menemenlis (2009), Simulated response of the Arctic freshwater budget to extreme NAO wind, *J. Clim.*, *22*, 2422–2437.

Conkright, M., R. Locarnini, H. Garcia, T. O'Brien, T. Boyer, C. Stephens, and J. Antonov (1989), *Geophysical Data Analysis: Discrete Inverse Theory*, *Int. Geophys. Ser.*, vol. 45, revised ed., 289 pp., Academic Press, San Diego, Calif.

Curry, J., J. Schramm, D. Perovich, and J. Pinto (2001), Application of SHEBA/FIRE data to evaluation of snow/ice albedo parameterizations, *J. Geophys. Res.*, *106*(D14), 15,345–15,355.

Daru, V., and C. Tenaud (2004), High order one-step monotonicity-preserving schemes for unsteady compressible flow calculations, *J. Comput. Phys.*, *193*(2), 563–594, doi:10.1016/j.jcp.2003.08.023.

Dmitrenko, I., I. Polyakov, S. Kirillov, L. Timokhov, I. Frolov, V. Sokolov, H. Simmons, V. Ivanov, and D. Walsh (2008), Toward a warmer arctic ocean: Spreading of the early 21st century Atlantic Water warm anomaly along the Eurasian Basin margins, *J. Geophys. Res.*, *113*, C05023, doi:10.1029/2007JC004158.

Edwards, M., B. Coakley, D. Chayes, S. Okkonen, M. Rognstad, D. Stockwell, and T. Whitledge (1999), Arctic Basin insights 1: New data for the Amerasian Basin from SCICEX-99, *Eos Trans. AGU*, *80*(46), Fall Meet. Suppl., T31F-08.

Fahrbach, E., J. Meincke, S. Osterhus, G. Rohardt, U. Schauer, V. Tverberg, and J. Verduin (2001), Direct measurements of volume transports through Fram Strait, *Polar Res.*, *20*(2), 217–224.

Fenty, I. (2010), State estimation of the Labrador Sea with a coupled ocean/sea-ice adjoint model, Ph.D. thesis, 277 pp., Mass. Inst. of Technol., Cambridge, Mass.

Fox-Kemper, B., and D. Menemenlis (2008), Can large eddy simulation techniques improve mesoscale rich ocean models?, in *Ocean Modeling in an Eddying Regime*, *Geophys. Monogr. Ser.*, vol. 177, edited by M. Hecht and H. Hasumi, pp. 319–338, AGU, Washington, D. C.

Fox-Kemper, B., R. Ferrari, and R. Hallberg (2008), Parameterization of mixed layer eddies. Part I: Theory and diagnosis, *J. Phys. Oceanogr.*, *38*, 1145–1165, doi:10.1175/2007JPO3792.1.

Gerdes, R., and C. Köberle (2007), Comparison of Arctic sea ice thickness variability in IPCC climate of the 20th centrury experiments and in ocean–sea ice hindcasts, *J. Geophys. Res.*, *112*, C04S13, doi:10.1029/2006JC003616.

Gouretski, V. V., and K. P. Koltermann (2004), WOCE Global Hydrographic Climatology, http://odv.awi.de/en/data/ocean/woce_global_hydrographic_climatology/, Ocean Data View, Hamburg, Germany.

Harder, M., and H. Fischer (1999), Sea ice dynamics in the Weddell Sea simulated with an optimized model, *J. Geophys. Res.*, *104*(C5), 11,151–11,162.

Heimbach, P., D. Menemenlis, M. Losch, J.-M. Campin, and C. Hill (2010), On the formulation of sea-ice models. Part 2: Lessons from multi-year adjoint sea ice export sensitivities through the Canadian Arctic Archipelago, *Ocean Modell.*, *33*, 145–158.

Hibler, W., III (1979), A dynamic thermodynamic sea ice model, *J. Phys. Oceanogr.*, *9*, 815–846.

Holland, M., J. Finnis, and M. Serreze (2006), Simulated Arctic Ocean freshwater budgets in the twentieth and twenty-first centuries, *J. Clim.*, *19*, 6221–6242.

Holloway, G., and Z. Wang (2009), Representing eddy stress in an Arctic Ocean model, *J. Geophys. Res.*, *114*, C06020, doi:10.1029/2008JC005169.

Holloway, G., et al. (2007), Water properties and circulation in Arctic Ocean models, *J. Geophys. Res.*, *112*, C04S03, doi:10.1029/2006JC003642.

Hopkins, T., M. Moustafa, C. Kinder, and M. Cook (1998), SCICEX-96 hydrographic data report, USS POGY SSN 647 polar cruise 27 August to 12 November 1996, *MEAS/NCSU Tech. Rep. 98-1*, N. C. State Univ., Raleigh.

Huffman, G. J., R. F. Adler, M. M. Morrissey, S. Curtis, R. Joyce, B. McGavock, and J. Susskind (2001), Global precipitation at one-degree daily resolution from multi-satellite observations, *J. Hydrometeorol.*, *2*, 36–50.

Jackett, D. R., and T. J. McDougall (1995), Minimal adjustment of hydrographic profiles to achieve static stability, *J. Atmos. Oceanic Technol.*, *12*, 381–389.

Johnson, M., S. Gaffigan, E. Hunke, and R. Gerdes (2007), A comparison of Arctic Ocean sea ice concentration among the coordinated AOMIP model experiments, *J. Geophys. Res.*, *112*, C04S11, doi:10.1029/2006JC003690.

Karcher, M., F. Kauker, R. Gerdes, E. Hunke, and J. Zhang (2007), On the dynamics of Atlantic Water circulation in the Arctic Ocean, *J. Geophys. Res.*, *112*, C04S02, doi:10.1029/2006JC003630.

Kauker, F., T. Kaminski, M. Karcher, R. Giering, R. Gerdes, and M. Vossbeck (2009), Adjoint analysis of the 2007 all time Arctic sea-ice minimum, *Geophys. Res. Lett.*, *36*, L03707, doi:10.1029/2008GL036323.

Kemp, J., K. Newhall, W. Ostrom, R. Krishfield, and A. Proshutinsky (2005), The Beaufort Gyre observing system 2004: Mooring recovery and deployment operations in pack ice, *Tech. Rep. WHOI-2005-5*, Woods Hole Oceanogr. Inst., Woods Hole, Mass.

Kwok, R. (2006), Exchange of sea ice between the Arctic Ocean and the Canadian Arctic Archipelago, *Geophys. Res. Lett.*, *33*, L16501, doi:10.1029/2006GL027094.

Kwok, R. (2009), Outflow of Arctic Ocean sea ice into the Greenland and Barents seas: 1979–2007, *J. Clim.*, *22*, 2438–2457, doi:10.1175/2008JCLI2819.1.

Kwok, R., and D. Rothrock (1999), Variability of Fram Strait ice flux and North Atlantic Oscillation, *J. Geophys. Res.*, *104*(C3), 5177–5189.

Kwok, R., A. Schweiger, D. Rothrock, S. Pang, and C. Kottmeier (1998), Sea ice motion from satellite passive microwave imagery assessed with ERS SAR and buoy motions, *J. Geophys. Res.*, *103*(C4), 8191–8214.

Kwok, R., G. Cunningham, and S. Pang (2004), Fram Strait sea ice outflow, *J. Geophys. Res.*, *109*, C01009, doi:10.1029/2003JC001785.

Langseth, M., T. Delaca, G. Newton, B. Coakley, R. Colony, J. Gossett, C. May, P. McRoy, J. Morison, WillamSmethie, D. Steele, and W. Tucker (1993), SCICEX-93: Arctic cruise of the US Navy nuclear powered submarine USS Pargo, *Mar. Technol. Soc. J.*, *27*, 4–12.

Large, W., and S. Yeager (2004), Diurnal to decadal global forcing for ocean and sea-ice models: The data sets and flux climatologies, *Tech. Note NCAR/TN-460+STR*, Natl. Cent. for Atmos. Res., Boulder, Colo.

Large, W. G., J. C. McWilliams, and S. Doney (1994), Oceanic vertical mixing: A review and a model with a nonlocal boundary layer parameterization, *Rev. Geophys.*, *32*(4), 363–403.

Leith, C. E. (1996), Stochastic models of chaotic systems, *Phys. D*, *98*, 481–491.

Lindsay, R., and J. Zhang (2006), Assimilation of ice concentration in an ice-ocean model, *J. Atmos. Oceanic Tech.*, *23*, 742–749.

Locarnini, R. A., A. V. Mishonov, J. I. Antonov, T. P. Boyer, and H. E. Garcia (2006), *World Ocean Atlas* 2005, vol. 1, *Temperature*, *NOAA Atlas NESDIS*, vol. 61, edited by S. Levitus, 182 pp., NOAA, Silver Spring, Md.

Losch, M., D. Menemenlis, P. Heimbach, J.-M. Campin, and C. Hill (2010), On the formulation of sea-ice models. Part 1: Effects of different solver implementations and parameterizations, *Ocean Modell.*, *33*, 129–144.

Manizza, M., M. J. Follows, S. Dutkiewicz, J. W. McClelland, D. Menemenlis, C. N. Hill, A. Townsend-Small, and B. J. Peterson (2009), Modeling transport and fate of riverine dissolved organic carbon in the Arctic Ocean, *Global Biogeochem. Cycles*, *23*, GB4006, doi:10.1029/2008GB003396.

Marshall, J., A. Adcroft, C. Hill, L. Perelman, and C. Heisey (1997), A finite-volume, incompressible Navier-Stokes model for studies of the ocean on parallel computers, *J. Geophys. Res.*, *102*(C3), 5753–5766.

Martin, T., and R. Gerdes (2007), Sea ice drift variability in Arctic Ocean model intercomparison project models and observations, *J. Geophys. Res.*, *112*, C04S10, doi:10.1029/2006JC003617.

Maslowski, W., D. Marble, W. Walczowski, U. Schauer, J. L. Clement, and A. J. Semtner (2004), On climatological mass, heat, and salt transports through the Barents Sea and Fram Strait from a pan-Arctic coupled ice-ocean model simulation, *J. Geophys. Res.*, *109*, C03032, doi:10.1029/2001JC001039.

Menemenlis, D., I. Fukumori, and T. Lee (2005a), Using Green's functions to calibrate an ocean general circulation model, *Mon. Weather Rev.*, *133*, 1224–1240.

Menemenlis, D., et al. (2005b), NASA supercomputer improves prospects for ocean climate research, *Eos Trans. AGU*, *86*(9), 89, 95–96.

Menemenlis, D., J. Campin, P. Heimbach, C. Hill, T. Lee, A. Nguyen, M. Schodlock, and H. Zhang (2008), ECCO2: High resolution global ocean and sea ice data synthesis, *Mercator Ocean Q. Newsl.*, *31*, 13–21.

Menke, W. (1989), *Geophysical Data Analysis: Discrete Inverse Theory*, *Int. Geophys. Ser.*, vol. 45, 289 pp., Academic Press, San Diego, Calif.

Miller, P., S. Laxon, D. Feltham, and D. Cresswell (2006), Optimization of a sea ice model using basinwide observations of Arctic sea ice thickness, extent, and velocity, *J. Clim.*, *19*, 1089–1108.

Nechaev, D., M. Yaremchuk, and M. Ikeda (2004), Decadal variability of circulation in the Arctic Ocean retrieved from climatological data by a variational method, *J. Geophys. Res.*, *109*, C04006, doi:10.1029/2002JC001740.

Nguyen, A., D. Menemenlis, and R. Kwok (2009), Improved modeling of the Arctic halocline with a subgrid-scale brine rejection parameterization, *J. Geophys. Res.*, *114*, C11014, doi:10.1029/2008JC005121.

Onogi, K., et al. (2007), The JRA-25 reanalysis, *J. Meteorol. Soc. Jpn.*, *85*(3), 369–432.

Panteleev, G., D. Nechaev, A. Proshutinsky, R. Woodgate, and J. Zhang (2010), Reconstruction and analysis of the Chukchi Sea circulation in 1990–1991, *J. Geophys. Res.*, *115*, C08023, doi:10.1029/2009JC005453.

Parkinson, C., and D. Cavalieri (2008), Arctic sea ice variability and trends, 1979–2006, *J. Geophys. Res.*, *113*, C07003, doi:10.1029/2007JC004558.

Paulson, C. A., and J. J. Simpson (1977), Irradiance measurements in the upper ocean, *J. Phys. Oceanogr.*, *7*, 952–956.

Rollenhagen, K., R. Timmermann, T. Janjic, J. Schroeter, and S. Danilov (2009), Assimilation of sea ice motion in a finite-element sea ice model, *J. Geophys. Res.*, *114*, C05007, doi:10.1029/2008JC005067.

Rothrock, D., and M. Wensnahan (2007), The accuracy of sea-ice drafts measured from U.S. Navy submarines, *J. Oceanic Atmos. Technol.*, *24*, 1936–1949.

Rothrock, D., W. Maslowski, D. Chayes, G. Flato, and J. Grebmeier (1999), Arctic Ocean science from submarines. A report based on the SCICEX 2000 workshop, report, Appl. Phys. Lab., Univ. of Wash., Seattle, Wash.

Rudels, B., E. Jones, U. Schauer, and P. Eriksson (2004), Atlantic sources of the Arctic Ocean surface and halocline waters, *Polar Res.*, *23*(2), 181–208.

Schauer, U., and E. Fahrbach (2004), Arctic warming through the Fram Strait: Oceanic heat transport from 3 years of measurements, *J. Geophys. Res.*, *109*, C06026, doi:10.1029/2003JC001823.

Serreze, M., A. Barrett, A. Slater, R. Woodgate, K. Aagaard, R. Lammers, M. Steele, R. Moritz, M. Meredith, and C. M. Lee (2006), The large-scale freshwater cycle of the Arctic, *J. Geophys. Res.*, *111*, C11010, doi:10.1029/2005JC003424.

Smith, W. H. F., and D. T. Sandwell (1997), Global sea floor topography from satellite altimetry and ship depth soundings, *Science*, *277*(5334), 1956–1962.

Spall, M. (2007), Circulation and water mass transformation in a model of the Chukchi Sea, *J. Geophys. Res.*, *112*, C05025, doi:10.1029/2005JC003364.

Spreen, G., L. Kaleschke, and G. Heygster (2008), Sea ice remote sensing using AMSR-E 89-GHz channels, *J. Geophys. Res.*, *113*, C02S03, doi:10.1029/2005JC003384.

Stark, J., J. Ridley, M. Martin, and A. Hines (2008), Sea ice concentration and motion assimilation in a sea ice-ocean model, *J. Geophys. Res.*, *113*, C05S91, doi:10.1029/2007JC004224.

Steele, M., J. Zhang, D. Rothrock, and H. Stern (1997), The force balance of sea ice in a numerical model of the Arctic Ocean, *J. Geophys. Res.*, *102*(C9), 21,061–21,079.

Steele, M., R. Morley, and W. Ermold (2001), PHC: A global ocean hydrography with a high-quality Arctic Ocean, *J. Clim.*, *14*, 2079–2087.

Uppala, S. M., et al. (2005), The ERA-40 re-analysis, *Q. J. R. Meteorol. Soc.*, *131*, 2961–3012.

Vinje, T., N. Nordlund, and A. Kvambekk (1998), Monitoring ice thickness in Fram Strait, *J. Geophys. Res.*, *103*(C5), 10,437–10,449.

Witte, H., and E. Fahrbach (2005), AWI Moored ULS Data, Greenland Sea and Fram Strait, 1991–2002, http://nsidc.org/data/g02139.html, Natl. Snow and Ice Data Cent., Boulder, Colo.

Woodgate, R., and K. Aagaard (2005), Revising the Bering Strait freshwater flux into the Arctic Ocean, *Geophys. Res. Lett.*, *32*, L02602, doi:10.1029/2004GL021747.

Woodgate, R., K. Aagaard, and T. Weingartner (2005), Monthly temperature, salinity, and transport variability of the Bering Strait through flow, *Geophys. Res. Lett.*, *32*, L04601, doi:10.1029/2004GL021880.

Woodgate, R., K. Aagaard, and T. Weingartner (2006), Interannual changes in the Bering Strait fluxes of volume, heat and freshwater between 1991 and 2004, *Geophys. Res. Lett.*, *33*, L15609, doi:10.1029/2006GL026931.

Wunsch, C. (2006), *Discrete Inverse and State Estimation Problems*, 1st ed., 384 pp., Cambridge Univ. Press, Cambridge, U. K.

Zhang, J., and W. D. Hibler (1997), On an efficient numerical method for modeling sea ice dynamics, *J. Geophys. Res.*, *102*(C4), 8691–8702.

Zhang, J., and D. Rothrock (2003), Modeling global sea ice with a thickness and enthalpy distribution model in generalized curvilinear coordinates, *Mon. Weather Rev.*, *131*, 681–697.

Zhang, J., and M. Steele (2007), Effect of vertical mixing on the Atlantic Water layer circulation in the Arctic Ocean, *J. Geophys. Res.*, *112*, C04S04, doi:10.1029/2006JC003732.

Zhang, J., D. Thomas, D. Rothrock, R. Lindsay, and Y. Yu (2003), Assimilation of ice motion observations and comparisons with submarine ice thickness data, *J. Geophys. Res.*, *108*(C6), 3170, doi:10.1029/2001JC001041.

R. Kwok, D. Menemenlis, and A. T. Nguyen, Jet Propulsion Laboratory, California Institute of Technology, MS 300-323, 4800 Oak Grove Dr., Pasadena, CA 91109-8099, USA. (ronald.kwok@jpl.nasa.gov; dimitris.menemenlis@jpl.nasa.gov; an.t.nguyen@jpl.nasa.gov)